Stony Brook University

Towards Single Photon Nonlinearities using Cavity EIT

A Thesis presented

by

Zakary Neumann Burkley

to

The Graduate School

in Partial Fulfillment of the

Requirements

for the Degree of

Master of Arts

in

Physics

Stony Brook University

August 2014

Stony Brook University

The Graduate School

Zakary Neumann Burkley

We, the thesis committee for the above candidate for the

Master of Arts degree, hereby recommend

acceptance of this thesis

Dr. Eden Figueroa - Thesis Advisor
Research Field: Atomic, Molecular, and Optical Physics, Quantum Electronics
Assistant Professor
Department of Physics and Astronomy

Dr. Thomas Allison - Inside Research Field Reader
Research Field: Atomic, Molecular, and Optical Physics, Quantum Electronics
Assistant Professor
Department of Physics and Astronomy

Dr. Rosalba Perna - Outside Research Field Reader
Research Field: Astronomy
Associate Professor
Department of Physics and Astronomy

This thesis is accepted by the Graduate School

Charles Taber
Dean of the Graduate School

Abstract of the Thesis

Towards Single Photon Nonlinearities using Cavity EIT

by

Zakary Neumann Burkley

Master of Arts

in

Physics

Stony Brook University

2014

In third order nonlinear mediums, the intensity of one optical field can modify the phase of another optical field [16]. This is known as cross-phase modulation (XPM) and is important for Quantum Information Processing (QIP) as phase shifts of single-photons that exceed π rad can be used to implement two-qubit quantum logic gates [20]. For a conventional XPM scheme, the Kerr nonlinearity responsible for XPM is too small for appreciable phase shifts to be achieved with low intensity optical fields. However, Electromagnetically Induced Transparency (EIT) can increase this nonlinearity by several orders of magnitude [19]. This thesis discusses the experimental construction of a laser-atomic system capable of EIT modulated XPM. This includes construction of a rubidium magneto-optical trap (RbMOT), characterization of this RbMOT, demonstration of EIT in the RbMOT, and a system capable of detecting optical phase shifts produced by EIT. The thesis concludes with an outlook on further implementations to the experiment that will increase this nonlinearity such that electric field phase shifts at the single-photon level are possible.

Dedicated to Dr. Joseph Ucchino

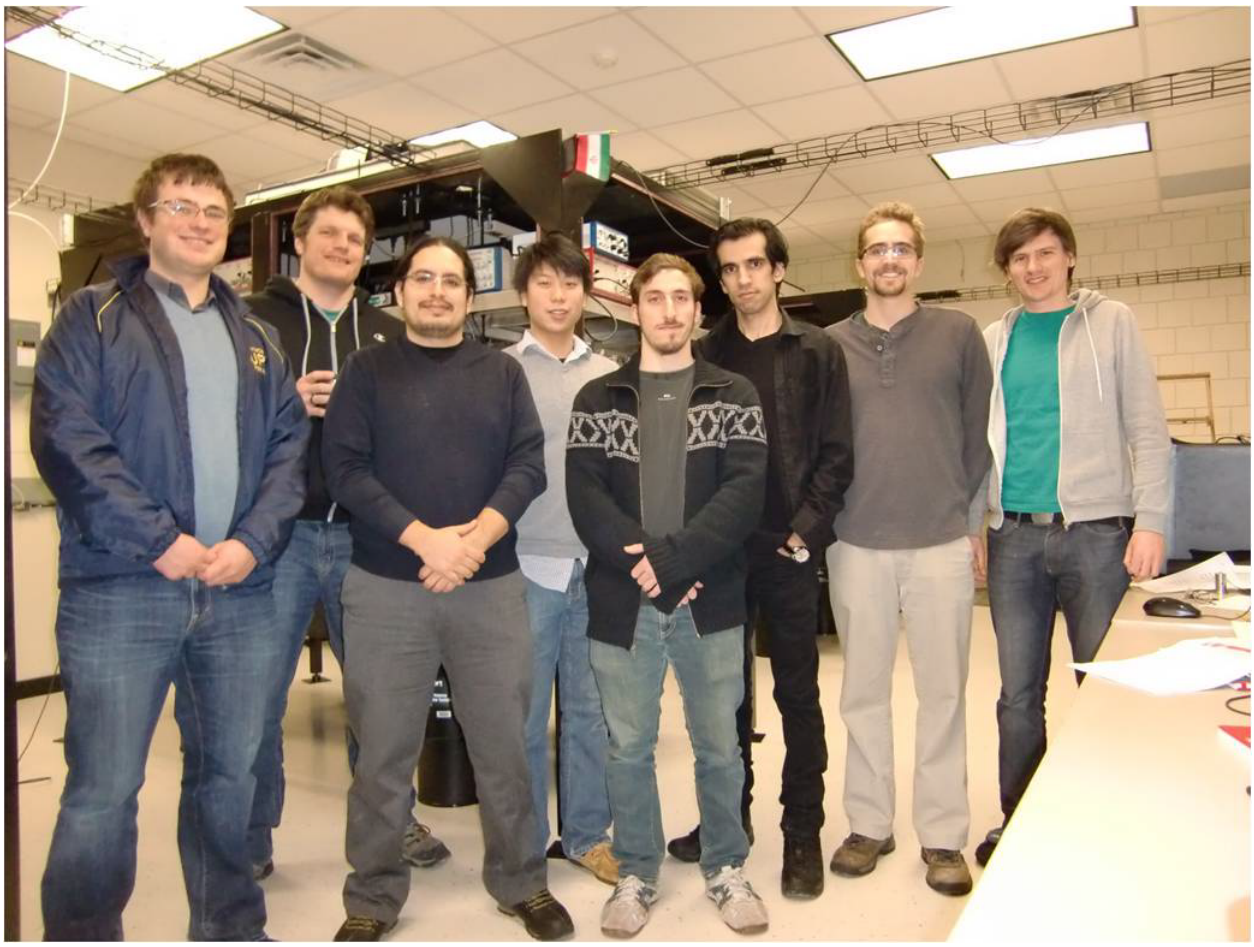

Contents

List of Figures

Preface

This thesis discusses the research I conducted in Professor Eden Figueroa's Quantum Information Technology Group from September 2013 - July 2014.

Acknowledgements

For those that helped me along the way, thank you.

Chapter 1

Introduction

According to Moore's Law, the number of transistors capable of being placed on a chip doubles every 18 months. Extrapolating this data suggests that the one atom-per-bit level could be reached by 2020 (see Figure 1.1) [1]. At this level classical computers would have to take into account quantum mechanical effects; quantum information technology (QIT) would be required to either replace and/or supplement current classical information technology. Whether or not classical computing can continue to progress without implementing QIT is debateable. Regardless, in this age of information, new avenues of information processing should be continually explored; current research illuminates QIT as a very promising avenue [4].

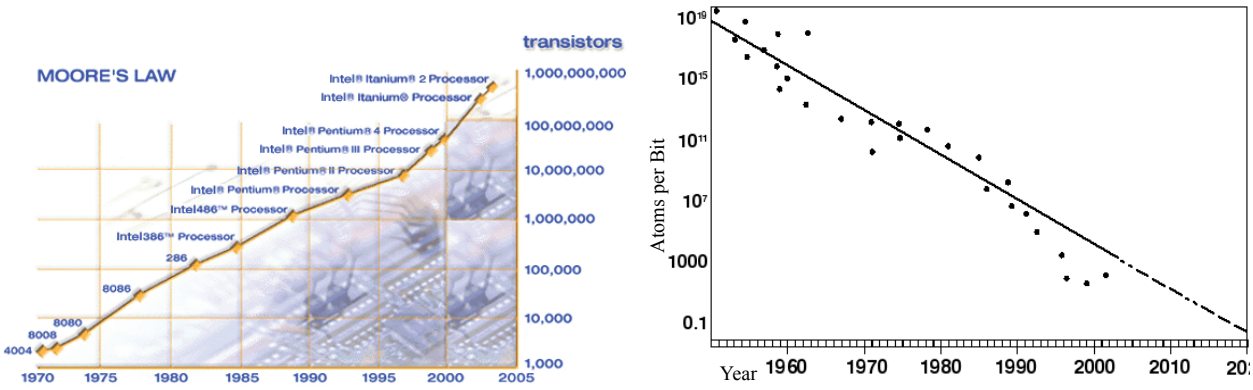

(a) Confirmation of Moore's Law from Intel computer chips

(b) The number of atoms per bit is approaching one. At this level quantum mechanical effects must be considered.

Figure 1.1: The size of classical computer technology is approaching the quantum level. Taken from [1].

Instead of just supplementing classical information technology, QIT can provide a brand new avenue of information processing, called quantum information processing (QIP). The

linearity of the Schrodinger equation requires that any linear combination of particular solutions is also a solution. This leads to the quantum mechanical superposition principle, which dictates that physical systems can be in a superposition of the system's possible eigenstates. So far this is not unique from classical wave equations that are also linear and permit superposition. What makes quantum superposition states distinguishable is that upon measurement the state collapses to a single eigenstate. This can be exploited to realize a novel type of information processing that has the potential to outperform current computer technologies. This is the motivation for QIP, where classical bits, which are in a definite state of 0 or 1, are replaced with quantum bits (qubits), which are in any superposition of 0 and 1 at the same time. To process information in this form would require the creation of a quantum computer built upon quantum processors. In such a device, the processors could evolve initial superpositions of qubits into different superpositions. Therefore, all information contained within these qubits is evolved simultaneously, resulting in parallel computation within a single processor. Classically, such computation could only be achieved with many discrete processors working in parallel. This 'quantum parallelism' enables computational tasks unrealistic classically. One prime example of such a task would be a quantum computer's ability to factor products of large prime numbers much faster than classical computers, putting the widely used RSA encryption methods at risk. Another application that emerges from QIP is quantum cryptography, which allows the unconditional secure transmission of messages by allowing the presence of an eavesdropper to be detected [2].

Qubits are physically realizable through the polarization states of a single photon, as well as numerous other physical systems [4]. Analogous to the binary states 0 or 1, photons that are in a superposition polarization state of Horizontal $|H\rangle$ and Vertical $|V\rangle$ can carry the quantum superpositions states that define a qubit. In this thesis, the term optical qubit will refer to the quantum information contained by the superposition polarization state of a single photon. Photons are attractive information carriers for QIP because light is robust in its ability to transport information. This is due to light's weak interaction with its surroundings, allowing it to travel long distances without decohering [5]. However, this strength is also a weakness. If we want to build a quantum computer with light we will need a quantum processor and thus quantum logic gates. Such logic gates will require one optical qubit to manipulate the state of another optical qubit. For optical qubits, this entails selectively modifying the phase of the electric field of a target qubit with a signal qubit. This could be envisioned as manipulating the polarization of the target qubit from $|H\rangle + |V\rangle$ to $|H\rangle - |V\rangle$, i.e., a 90^o selective phase shift for the vertical component of the oscillating electric field. Although light cannot directly manipulate light, there are atom-light interactions that make this possible.

Through the optical Kerr effect, the intensity of one light field can change the index of refraction seen by another light field and hence its phase, this is called cross-phase modulation (XPM) [16]. This effect; however, is not the only tool needed to develop an optical two-qubit quantum phase gate. This is because the optical Kerr effect relies on a nonlinear term that couples light's interaction to an atomic medium; the coefficient of this term is approximately $10^{-15}\mathrm{m}^2/\mathrm{V}^2$ for the atomic gases used for optical quantum information. Because of this, this effect can only been seen with very intense light fields, which are very far away from the single-photon level we desire. We need an additional tool to exaggerate the optical Kerr effect. This tool is Electromagnetically Induced Transparency [19].

Electromagnetically Induced Transparency (EIT) uses two coherent light sources, e.g., lasers, to prevent excitation to the single excited state of a three level atom. Since atoms in the ground states cannot be excited to this state, the atoms are transparent to light as they cannot undergo absorption [3]. On top of this transparency, EIT drastically modifies other properties of the atomic medium, including increasing nonlinearities. Therefore, combining EIT with the optical Kerr effect increases electric field phase shifts between two light fields.

An electric field phase shift of π rad between light fields at the single photon level is the ultimate goal towards which this thesis is working. If achieved, this would enable the construction of a deterministic two-qubit quantum logic gate [20]. The goal of this thesis was development of the necessary tools to achieve optically controlled interactions within a cold atomic ensemble that could be used to manipulate phase shifts between two light fields. This required four experimental tools:

1. **Theoretically**: A platform to mediate light-atom-light interactions.
   Experimental Implementation: Magneto-optically trapped rubidium atoms.

2. **Theoretically**: A tool to control light-atom-light interactions.
   Experimental Implementation: Electromagnetically induced transparency.

3. **Theoretically**: A way to implement and enhance optical phase shifts of electric fields.
   Experimental Implementation: Modification of electromagnetically induced transparency.

4. **Theoretically**: A method of measuring electric field phase shifts.
   Experimental Implementation: Balanced homodyne tomography.

The structure of this thesis mimics the list above, outlining the basic theory, experimental implementation, and measurements for each tool. **Chapter 2** discusses the basic theory of laser cooling and magneto-optical traps (MOTs). The required tools to experimentally implement these techniques and trap cold atoms are explained. Lastly, measurements

characterizing the number of cold atoms present in the MOT and their temperature are presented. **Chapter 3** begins with a derivation of the Hamiltonian for Electromagnetically Induced Transparency. Important consequences of this Hamiltonian are introduced, e.g., dark states, linear susceptibility, slow light, and cross-phase modulation. Here we describe the tools to experimentally achieve EIT and XPM in atomic systems. Measurements displaying our EIT spectrum and its optimization are presented. **Chapter 4** introduces the optical Kerr effect, self-phase modulation and cross-phase modulation (XPM). Improvement of conventional XPM through modification of EIT is examined. Implementing this improvement is explained and results showing modification of EIT are presented. Lastly, balanced homodyne tomography as a method of measuring electric field phase shifts is briefly introduced. A phase shift measurement through EIT is shown. **Chapter 5** concludes the thesis by examining the work done and introducing the next set of experimental tools that will be added to this work in order to achieve electric field phase shifts at the single photon level.

Chapter 2

MOT Theory

Motivation

An interface between states of light carrying quantum information and matter is essential for quantum information processing as it enables the storage and processing of this information [4]. Atomic ensembles are an attractive candidate for this interface as photons can interact strongly with systems containing a large number of atoms [5]. An experimental realization of such a system can be achieved with ultra cold alkali atoms. We choose cold atoms for two reasons. Physically, they have less decoherence than warm atoms as there are less collisions. Technically they allow easier implementation of cavities and EIT. The first demonstration of an ultra cold alkali atom-light interface storing and retrieving optical qubits was achieved using rubidium ensembles in 2005 [7]. Since this achievement, magneto-optically trapped alkali atoms have been utilized in a variety of quantum information experiments regarding storage, retrieval, entanglement and processing of optical single qubits [8]. Therefore, using cooled rubidium in a magneto-optical trap as our interface for processing optical qubits through phase shifts, we will be able to build upon the existing research in the field. We hope to add to this research by developing the first two qubit atom-light interface.

2.1 MOT Theory

2.1.1 Introduction to Laser Cooling

We are taught in early science classes that temperature is determined by the motion of atoms. For a gas of non-interacting atoms, we only need to consider translational motion. This leads to the familiar relation between the root-mean-square (r.m.s.) velocity of atoms in a gas and their temperature

$$v^{rms} = \sqrt{\frac{3k_bT}{m}}, \tag{2.1}$$

where k_b is Boltzmann's constant, m is the individual mass of each atom, and T is the temperature in K. From this it is clear that slowing down atoms will cool them. What is not obvious is that Lasers can be used for this cooling. This can be accomplished by utilizing the mechanical force of light on gaseous atoms to slow down their speed. Once cooled, magnetic coils can trap these atoms at a specific point in space. Although Maxwell hypothesized that radiation has momentum in the 19^{th} century, and the first experimental demonstration of light-induced mechanical forces came in 1933, it wasn't until 1997 that the Nobel Prize for Physics was awarded for the cooling and trapping of neutral atoms with laser light [10][11]. The cooling was achieved utilizing the Doppler effect, whereas trapping can be accomplished through magnetic fields and the Zeeman effect. Combining Doppler Cooling with magnetic trapping a Magneto-Optical Trap (MOT) can be created. The theoretical components that are the basis of this MOT follow.

2.1.2 Doppler Cooling: Conceptual Explanation

Consider an atom moving in the $+x$ direction. If we hit this atom head-on with a counterpropagating laser beam of frequency $\nu_L = \nu_o + \delta$, where ν_o is the resonant frequency of the atom's transition and δ is the laser detuning, we will find that a detuning of zero does not correspond to a transition for some velocity classes. This is because in the rest frame of the atom, the laser has a Doppler shifted frequency

$$\nu_L^{'} = \nu_L \left(1 + \frac{v_x}{c}\right) \approx \nu_o + \delta + \frac{v_x}{c}\nu_o, \tag{2.2}$$

where we have assumed $\delta \ll \nu_o$ and $v_x \ll c$ [11]. Therefore, tuning our laser off-resonance such that $\delta = -\frac{v_x}{c}\nu_o$, we can cause our light to be absorbed on-resonance with the atom. Since our laser beam is travelling in the $-x$ direction, each time the atom absorbs a photon it will recoil in the propagation direction of the light. However, when the atom spontaneously emits the photon, the atom's direction change from this will average out to zero since each photon will be kicked off in a random direction. This leads to a net momentum change in the atom of

$$\Delta p_x = -\frac{h}{\lambda}. \tag{2.3}$$

This simple explanation suggests that with enough photon absorptions the atom's motion can be completely stopped. However, a more in depth treatment reveals that the recoil from

spontaneous emission cannot be ignored, putting a bound on the minimum temperature possible through Doppler Cooling.

2.1.3 Scattering Force and Optical Molasses

As we saw in the previous heuristical explanation, light can lessen the momentum of an atom moving in a specific direction. For a single atom we saw that this decrease was just the momentum of a single photon. We are not working with single atoms, and we cannot assume that all photons are absorbed by each atom. It therefore makes sense to consider a population of atoms and the rate at which they absorb photons. For a two-level atom, which we can approximate very closely using the hyperfine levels of rubidium, the scattering rate is given by

$$R_{scatt} = \frac{\Gamma}{2} \frac{\Omega^2/2}{\delta^2 + \Omega^2/2 + \Gamma^2/4}, \tag{2.4}$$

where $\Gamma = 1/\tau$ is the radiative decay of the atom (τ is the excited state lifetime), Ω is the Rabi Frequency (the oscillation of population between the two levels), and $\delta = \omega - \omega_o + kv$ is the doppler accounted detuning between atomic resonance, ω_o, and the laser frequency, ω for an atom with velocity v along the same direction as the photon wave vector k [12]. Using the useful relation $I/I_{sat} = 2\Omega^2/\Gamma^2$, where I is the laser intensity and I_{sat} is the saturation intensity at which the laser drives the excited state population to equal the ground state, we can write the scattering force as

$$\begin{aligned} F_{scatt} &= (\text{photon momentum}) \, \text{x} \, (R_{scatt}) \\ &= \hbar k \frac{\Gamma}{2} \frac{I/I_{sat}}{1 + I/I_{sat} + 4\delta^2/\Gamma^2}. \end{aligned} \tag{2.5}$$

So far this derivation has assumed an atomic beam in a specific direction, slowed down by a counterpropagating laser beam. However, our system is an atomic gas. This requires three cooling laser beams along the x, y, and z dimensions, where the beams are retroreflected to slow atoms from both the positive and negative direction of each dimension. This is called Optical Molasses in analogy to a particle trapped in a viscous fluid. In our case, light acts as the fluid, putting a damping mechanical force on our particle (atom) from all directions. For one specific direction the force is the sum of the scattering force for positively and negatively doppler shifted atoms

$$
\begin{aligned}
F_{molasses} &= F_{scatt}(\omega - \omega_o - kv) + F_{scatt}(\omega - \omega_o + kv) \\
&\approx F_{scatt}(\omega - \omega_o) - kv\frac{\partial F_{scatt}}{\partial \omega} - \left(F_{scatt}(\omega - \omega_o) + kv\frac{\partial F_{scatt}}{\partial \omega}\right) \\
&= -2\frac{\partial F_{scatt}}{\partial \omega}kv \\
&= -\alpha v,
\end{aligned}
\tag{2.6}
$$

where $\alpha = 2k\frac{\partial F_{scatt}}{\partial \omega}$ is the damping coefficient, which from (2.5) is

$$
\alpha = 4\hbar k^2 \frac{I}{I_{sat}} \frac{-2\delta/\Gamma}{\left(1 + I/I_{sat} + 4\delta^2/\Gamma^2\right)^2}. \tag{2.7}
$$

We see from this molasses force that atoms trying to escape the intersection of all three beams will experience a scattering force opposite their direction of motion that increases with their velocity. This leads to the desired result of accumulating slowed atoms at the intersection of all three beams and their retroreflections.

2.1.4 Doppler Cooling Limit

Although (2.6) implies a velocity of zero for balanced molasses forces, there is a limit to the temperature attainable via Doppler cooling. This is due to the heating effect of the spontaneously emitted photons. Since each emission is in a random direction, the atom will randomly move around the intersection point of the molasses beams. If N is large, then after N absorption-emission cycles the average momentum of this random movement will be zero, the momentum squared will be

$$
\bar{p_i^2} = 2\left(2N\hbar^2k^2\right), \tag{2.8}
$$

where the first 2 accounts for the laser beam and its retroreflection, and the second 2 for the fact that the atom experiences a momentum change double the momentum of a single photon [12]. This is because when emitted, the photon and atom recoil in opposite directions. Therefore, the energy of heating is

$$
\left(\frac{dE}{dt}\right)_{heat} = \frac{1}{2m}\frac{d\bar{p_i^2}}{dt} = \frac{2\hbar^2k^2R_{scatt}}{m}. \tag{2.9}
$$

From (2.6) we see that the change in energy from cooling is

$$
\left(\frac{dE}{dt}\right)_{cool} = F_i v_{rms_i} = -\alpha v_i^2. \tag{2.10}
$$

By conservation of energy, the change in energy from heating and cooling must equal zero. Therefore we see that the minimum velocity we can reach by Doppler cooling is

$$v_i^2 = \frac{2\hbar^2 k^2 R_{scatt}}{m\alpha}. \tag{2.11}$$

From (2.1) we then see that the minimum temperature is:

$$\begin{aligned} T_{min} &= \frac{2\hbar^2 k^2 R_{scatt}}{k_b \alpha} \\ &= \frac{-\hbar\Gamma}{8k_b} \frac{(1 + I/I_{sat} + 4\delta^2/\Gamma^2)}{\delta/\Gamma}. \end{aligned} \tag{2.12}$$

In the limit $I \ll I_{sat}$ we see that the Doppler temperature limit simplifies to

$$T_{min} = \frac{\hbar}{2k_b\tau}, \tag{2.13}$$

for $\delta = -\Gamma/2$. For rubidium atoms this is approximately 150μK [9].

2.1.5 Magneto-optical Trapping

The optical molasses force is a function of velocity. This slows down atoms and causes them to collect near the intersection of all three beams. However, the atoms still diffuse out over a few seconds in time. To prevent this, there must also be a position dependent force that pushes the atom back towards the center of the cooling beams' intersection. This can be achieved through utilization of the Zeeman effect.

Using a pair of anti-helmholtz coils, where the currents flow in opposite directions, a quadrupole magnetic field can be created. Because of the opposite currents, the magnetic field is zero at the center that is surrounded by a uniform field gradient (see Figure 2.1) [11].

For a hypothetical transition of F=0 to F=1, where the F levels are the hyperfine atomic structure, the gradient will Zeeman split the $m_f = -1, 0, +1$ sublevels in the F=1 state. For $B < 0$ the $m_f = -1$ will be shifted up in energy while the $m_f = +1$ will be shifted down. The reverse is true for $B > 0$. Therefore, depending on the position of the atom, i.e., whether it experiences a $B > 0$ or $B < 0$ field, either $m_f = +1$ or $m_f = -1$ will be tuned closer to resonance with a red-detuned laser. For example, from the Figure 2.1, an atom moving in the $-z$ direction will be immersed in a $B > 0$ field. This will detune the $m_f = -1$ sublevel closer to resonance. The opposite case is true for atoms moving in the $+z$ direction. Now, $\Delta m_f = -1$ transitions must be addressed with left-handed circularly polarized light, σ^-, and $\Delta m_f = +1$ with right handed polarized light σ^+. Therefore, sending a σ^- beam in from the bottom and a σ^+ beam from the top creates an imbalance in the radiation force at

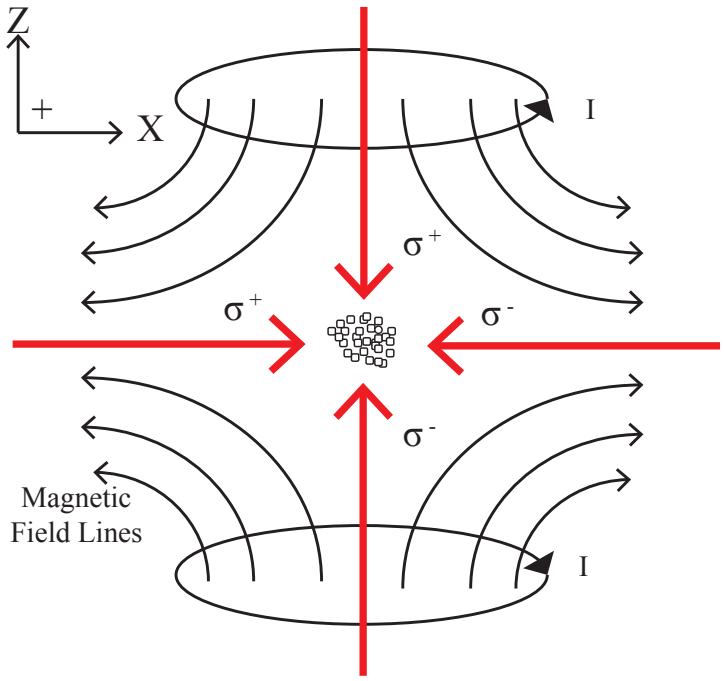

Figure 2.1: The currents cancel their respective magnetic fields at the center of the coils. Away from this zero point the magnetic field increases positively in the +x, -z directions and negatively in the -x, +z directions.

points away from B=0. Atoms moving in the $-z$ direction will absorb more light from the σ^- beam than the σ^+, resulting in a radiation forces towards $B = 0$, with the reverse case for atoms moving in the $+z$ direction. This explanation is depicted in Figure 2.2.

We see that the total force in our MOT is not only from optical molasses anymore, but also from the imbalanced radiation force caused by Zeeman splitting. This total force can be calculated similar to that of optical molasses, except that we now need to incorporate the frequency shift caused by Zeeman splitting:

$$\begin{aligned} F_{MOT} &= F_{molasses} + F_{zeeman} \\ &= F^{\sigma^+}_{scatt}(\omega - kv - (\omega_o + \beta z)) - F^{\sigma^-}_{scatt}(\omega + kv - (\omega_o - \beta z)) \\ &\approx -2\frac{\partial F}{\partial \omega} + 2\frac{\partial F}{\partial \omega_o}\beta z = -2\frac{\partial F}{\partial \omega}\left(kv - \beta z\right), \end{aligned} \tag{2.14}$$

where $\beta z = \frac{g\mu_B}{\hbar}\frac{dB}{dz}z$, is the Zeeman frequency shift at displacement z, μ_B is the Bohr magneton and g the Lande g-factor [12]. From before we know that $2k\frac{\partial F}{\partial \omega} = \alpha$. Using the fact that $\frac{\partial F}{\partial \omega_o} = -\frac{\partial F}{\partial \omega}$, since $\delta = \omega - \omega_o + kv$, we see that the total force on the atoms is

$$F_{MOT} = -\alpha v - \frac{\alpha\beta}{k}z. \tag{2.15}$$

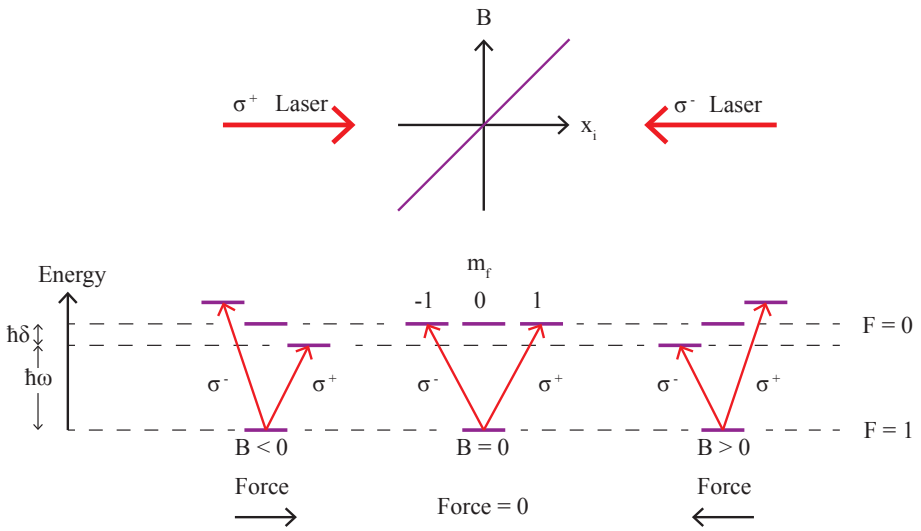

Figure 2.2: Schematic of the Zeeman Shift that causes radiation forces to push atoms towards the center. Sublevels with $m_f > 0$ are shifted up in energy for $B > 0$ and down in energy for $B < 0$. Sublevels with $m_f < 0$ are shifted up in energy for $B < 0$ and down in energy for $B > 0$. Depending on the position and direction of motion of an atom, one of the sublevels will then be shifted on resonance with the red-detuned laser propagating in the opposite direction as the atom. This causes an imbalance in the radiation force that pushes the atom towards the center where $B = 0$.

The imbalance in the radiation force caused by Zeeman splitting creates a position-dependent restoring force that pushes the cooled atoms to the center of the MOT. This completes our magneto-optical trap.

2.2 MOT Implementation

Implementing this theoretical framework and producing a MOT requires several experimental tools. A vacuum system is required to prevent interaction between the atmosphere molecules and cooled atoms. Anti-Helmholtz coils are needed for magnetic trapping. Atoms with level schemes that allow cooling are required. After the atoms are chosen, continuous wave lasers that can address the resonances of these atoms are needed. Along with this, some way to detune the lasers from resonance is also required. Furthermore, if we wish to perform measurements on the atoms in the MOT at their natural resonance, we need some way to pulse our cooling beams and trapping coils on and off, as they perturbate the atomic levels. Developing these experimental tools was the first several months work of this thesis. The description of this development follows.

2.2.1 Vacuum System and Magnetic Coils

Not evident from the main body of this thesis, but briefly explained in the outlook, the end goal of this experiment on which this thesis is working toward requires a very small vacuum cell (16mm by 16mm by 60mm). This is because we will build cavities around the vacuum cell to increase atom-light interaction. For the cavities to do this the vacuum cell must be a small volume so the distance between the cavities is not too large. Such a small vacuum system is extremely difficult to engineer. For this reason, we utilized a custom-made product from the company, ColdQuanta. The vacuum chamber is evacuated using a highly compact ion pump thus creating an ultra-high vacuum fitting the dimensions we were looking for. Embedded in the system is a rubidium source, from which we can load more atoms into the cell, and magnetic trapping anti-Helmholtz coils. Optical elements are added to achieve a 3-D laser cooling configuration (see Figure 2.3 and Figure 2.4). Additionally to these tools, the heart of laser cooling lies in developing a laser system able to address the atoms. This was a main focus of this thesis work.

2.2.2 Atomic Level Scheme

We are working with Rubidium 87 (Rb^{87}). With its first four shells filled, and only a single electron in its fifth shell, rubidium has a very simple level scheme that can be modeled well by two,three, and four level-atomic systems. Because of this, the properties of Rubidium are well understood. This helps explain why technology operating at Rb^{87}transitions is so robust. This has led to well-engineered lasers operating continuously at Rb^{87} transition frequencies. Besides it technological benefits, this atomic level scheme fits the requirements for laser cooling. Considering these facts, it is no surprise that rubidium is one the more commonly used atoms for laser cooling.

From the Maxwell-Boltzmann distribution, the root mean square speed of room temperature rubidium is approximately 290 m/s. From Equation 2.3, for Rb^{87} transitions at 780 nm transitions it would then take approximately $50,000$ photons to cool one rubidium atom to its Doppler Limit. This means $50,000$ absorption emission cycles. Therefore, for our cooling process to work we need some way to recycle our atoms, that is, prevent them from de-exciting to levels not on resonance with the cooling laser. Using the fine and hyperfine splitting of Rb^{87}, we create what is called a "closed cycling transition," as shown in Figure 2.5.

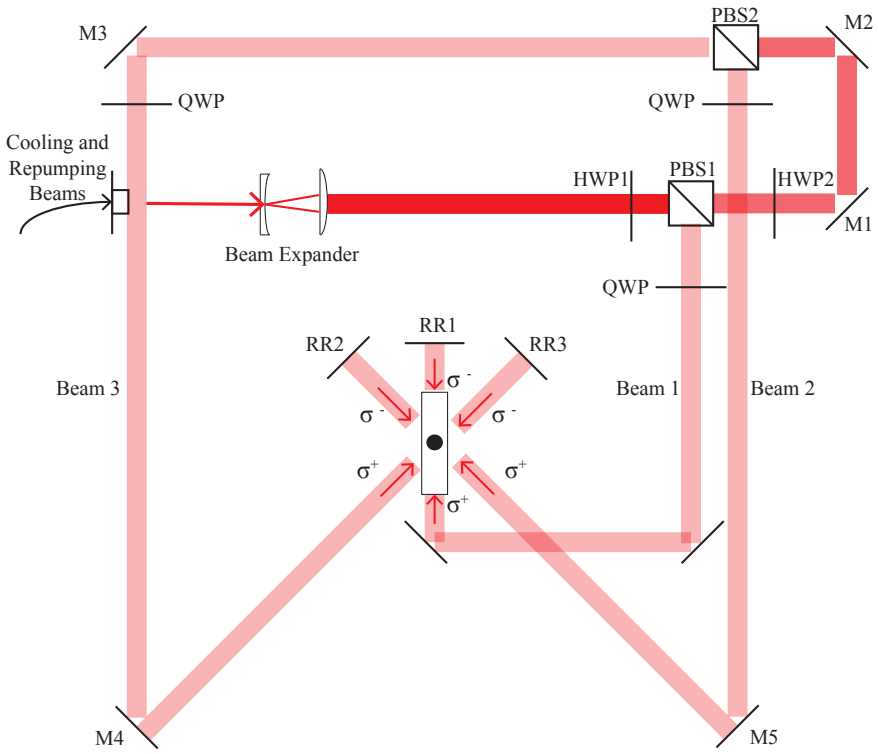

Figure 2.3: 2D schematic of 3D trapping configuration. Initially, the cooling/repumping beam are coupled into the same fiber. Once they exit this fiber they are expanded through a lens system. Then, through half-wave plate (HWF1), the polarization of the beam is adjusted so that 33% of the power exits at polarizing beam-splitter 1 (PBS1) to create Beam 1. The same process follows for Beam 2, except HWP2 is adjusted so that 50% of the remaining beam power is used. The 33% of the original power remaining is reflected towards the MOT using mirror 3 (M3) and is Beam 3. After PBS1, PBS2, and M3 a quarter-wave plate (QWP) is placed to put the beams into the correct circular polarization. Each beam then follows a path of mirrors to the MOT, where they are reverse direction at retro-reflectors 1,2,3 (RR1, RR2, RR3), with their polarization reversed in the process.

2.2.3 Laser Locking

We use two a Toptica tunable amplified diode lasers (TA-PRO) to address the $F = 2$ to $F' = 2$ and $F = 1$ to $F' = 2$ transitions. Each laser can output a maximum of 1.5 W. This provides ample power for our cooling beams (25 mW) and repumping beams (5 mW), phase lock (3 mW), and a large excess of remaining power to construct numerous beam pathways for further use in the experiment. To lock to the $F = 1$ to $F' = 2$ frequency we use a setup that provides a Doppler Free spectrum of Rubidium through saturated absorption spectroscopy. Inside our compact system is a vapour cell of Rubidium. A small part of light exiting a side port of the diode-laser is used in the spectroscopy setup. When we can scan the laser frequency we can obtain an image of the absorption spectrum of rubidium

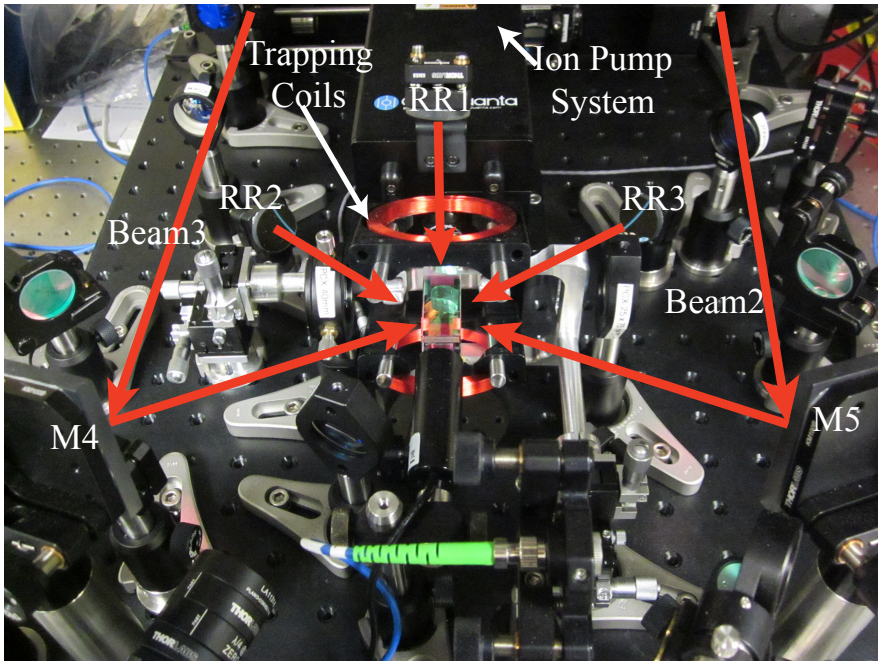

Figure 2.4: Photograph of MOT. Beams 2 and 3 are actually vertically higher than Beam 1, and are reflected into the vacuum cell at a downward angle. Beam 1 comes along near the bottom of the vacuum system, encounters a mirror, and then another mirror that reflects it directly vertical into the vacuum cell and eventually to RR1 (Only this reflection off RR1 is visible in this picture).

on our computer screens (see Figure 2.6). By modifying the laser frequency we can select our desired Doppler broadened transitions and the resolved hyperfine transition using the Doppler-free signal from the spectroscopy setup. The laser frequency can then be locked to this transition through a feedback loop system that continuously adjusts diode current and the piezo controlling the laser grating, maintaining our desired frequency constant over time.

To lock our second laser to the F=2 to F'=2 transition we use a technique called phase locking. As seen in Figure 2.7, each laser has some of its light coupled to a fiber. The light from both these fibers is then coupled into a single fiber. This creates a beat signal at the frequency difference between the lasers, which is too fast to manipulate with our electronics. To manipulate this signal we mix it down to the MHz level using a reference signal from an electronic oscillator at 6.891 GHz. This frequency is 80 MHz away from the difference between the F=1 and F=2 rubidium hyperfine states of 6.831 GHz. The resulting 80 MHz signal is then compared to a 80 MHz reference signal. A servo-loop assures that both signals remain in-phase by providing feedback to the current of the second diode-laser.

The diagram of the two laser set-up is shown in Figure 2.7. Immediately upon exiting the laser system, the light encounters a half-wave plate (HWP). These devices rotate linearly polarized light between horizontal, vertical, or a superposition of the two. They are always

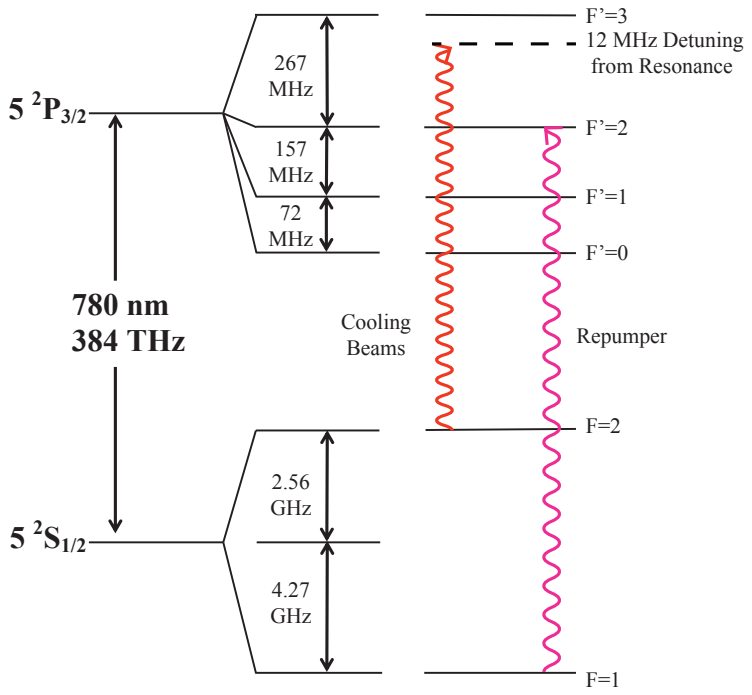

Figure 2.5: For this system the selection rules are $\Delta F = +/-1, 0$ (except a 0 to 0 transition). Exciting $F = 2$ to $F' = 3$, the only possible decay state is $F = 2$. Except for one caveat, this is our cycling transition. A small percentage of atoms from $F = 2$ will end up in $F' = 2$, where they can decay either to $F = 2$ where they will reenter the cycle, or $F = 1$ where they exit the cycle. We therefore need a repumping laser to pump atoms from $F = 1$ to $F' = 2$ where they will be continually recycled into the cycling transition, closing our system.

.

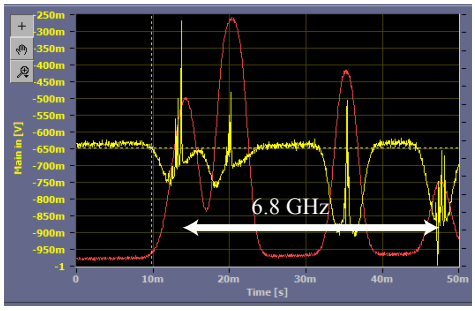

(a) Doppler Broadened Absorption Spectrum of Rubidium [Red] and Doppler Free Absorption Spectrum [Yellow] using a scan of ≈ 8GHz.

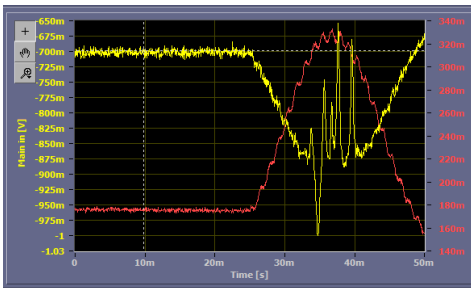

(b) Doppler Free Absorption spectrum of the Rubidium 87 F=2 to F' Transitions.

Figure 2.6: Saturated Absorption Spectroscopy of Rubidium. The time axis corresponds to the time it takes to pizeo-electrically adjust the diffraction grating which controls the frequency output of the laser.

found before a polarizing beamsplitter (PBS), as PBSs transmit horizontal polarization and reflect vertical polarization. Half-wave plates thus serve as way to modulate the power of the

two beam paths created after a PBS. The light is then reflected into a fiber coupler (FC) into a polarization maintaining optical fiber (PMF). If aligned correctly, light coupled into this fiber should not fluctuate in polarization upon exit, which is an issue as this causes power fluctuations after PBSs. Often, this correct coupling can be obtained by placing a polarizer in front of the fiber coupler, which only allows a defined polarization to enter.

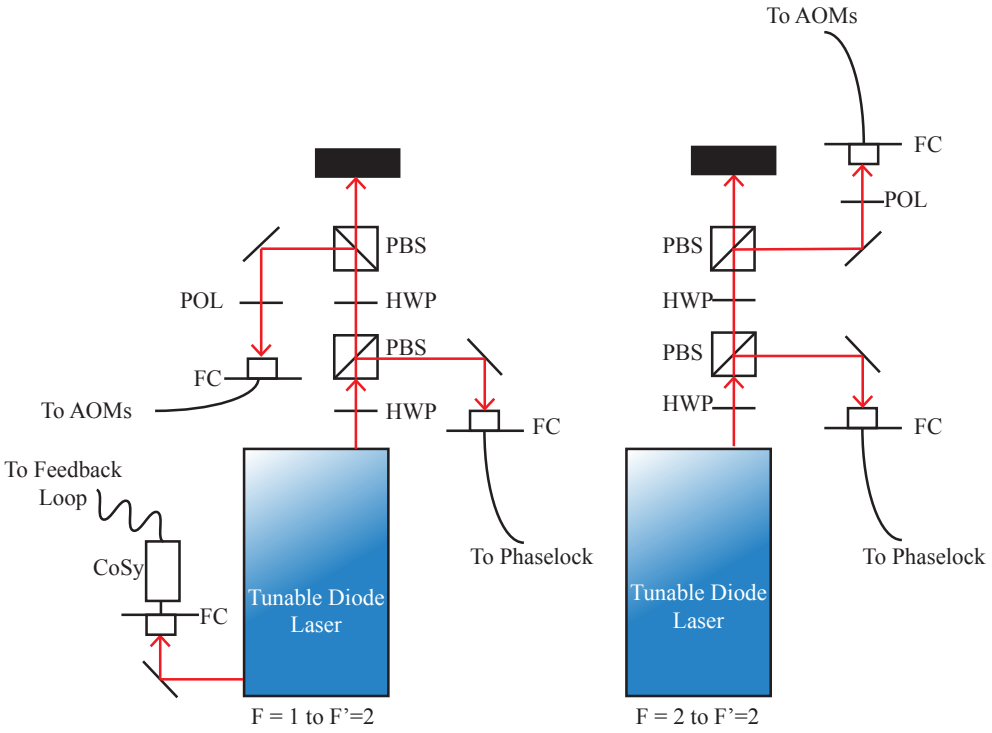

Figure 2.7: Two laser system required to create cooling cycling transition

.

2.2.4 Acousto-optic Modulators

The principle of Doppler Cooling relies on a cooling laser red-detuned from atomic resonance. Using the detuning from Equation 2.2 we get a rough estimate that we need to detune our lasers from around 10-30 MHz below atomic resonance of the F=2 to F'=3 transition. However, our phase lock locks our cooling laser frequency to the exact atomic resonance of the F=2 to F'=2 transition, which is 267 MHz below the F'=3 hyperfine level. We need a device that can shift the frequency of our lasers on the few hundred MHz level in order to hit correct transitions required for laser cooling. This is achieved through Acousto-optic modulation.

Acousto-optic Modulators (AOMs) are ubiquitous in Atomic, Molecular, and Optical (AMO) physics. AOMs consist of a transparent material, such as quartz, sandwiched between

an acoustic absorber and a piezo-electric transducer (see Figure 2.8).

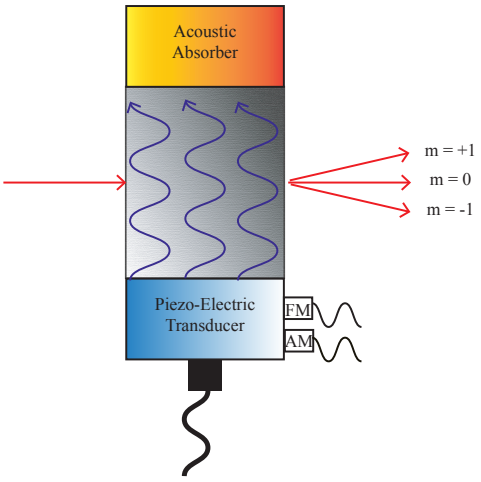

Figure 2.8: Sound waves (blue) created by a piezo-electric device pass through a quartz medium. Light (red) that enters from the left will experience a diffraction shift. The first order diffraction shifts are shown here as they are the ones relevant to the experiments we designed. The frequency of the sound wave that doppler shifts each order is controlled by a frequency modulation (FM) port. The intensity of this sound wave and the intensity of each order is controlled by an amplitude modulation (AM) port. Saturating the AM port, the AOM can be aligned such that the intensity of the first order beams reach 80 percent of the original beam's intensity.

An oscillating electric signal causes the transducer to vibrate, sending sound waves through the quartz medium. These waves expand and compress the quartz, changing its index of refraction. These periodic index modulations cause the light to diffract. Not only is the light diffracted, but each mode has its frequency doppler shifted by the sound wave such that $f_l = f_l + mf_s$, where m is the diffraction mode. This leads to $+/-$ frequency shifts depending on the propagation direction of the laser relative to the sound wave. Using these properties we can detune our laser from atomic resonance [16].

2.2.5 Pulsing

The trapping coils and cooling/repumping beams cause Zeeman splitting and an AC Stark shift for the cooled atoms, respectively. Therefore, as is common, to measure properties of the MOT atoms, we need some way to pulse our magnetic coils and cooling beams so we can observe the atomic cloud without these perturbing effects. The device we use to do this is the 9520 Digital Delay Pulse Generator built by Quantum Composers. This device has 8 independently digitally controlled channels where we can control the delay, width, rate, and amplitude of our pulses. We can also superimpose certain pulse sequences to create

more complex sequences. With a resolution of 250 ps, an accuracy of 1 ns, the device easily satisfies the μs precision requirements we have faced in the lab so far.

Pulsing the magnetic coils is accomplished through an electrical switch capable of switching a 1 amp current in less than 1 μs. Our coils are continuously on unless the switch receives a pulse. Pulsing the cooling/repumping beams requires further use of our AOMs. We cannot simply turn off the lasers, as our laser has been separated in numerous pathways, some that may still need to be on when the cooling/repumping beams are turned off. However, AOMs once again display their ubiquity in AMO labs as they can solve this problem.

As seen in Figure 2.9, after each AOM is an iris that only allows the diffraction mode with the desired frequency to pass through. When the AOM is on, only this diffraction mode passes through the iris, and the original beam, as it is not diffracted, ends it journey on the iris. When the AOM is off, no light passes through. Therefore, pulsing the amplitude modulation of our AOM acts an acousto-optical shutter. In this way we can "turn off" our laser light without actually turning off the laser. This technique works fine for our cooling beams, as we are using an AOM to increase our frequency that is locked to the $F = 2$ to $F' = 2$ transition so that it almost addresses the $F = 2$ to $F' = 3$ transition. However, our repumping beams are already locked to the correct frequency, meaning we can't use an AOM as we did with the cooling beams to act as an electrical shutter. There is a way around this using a double-pass AOM set-up where we shift the frequency of our beam up by taking the +1 diffraction mode as it passes through originally. Reflecting this mode off a mirror and back through the AOM we can take the -1 diffraction mode, producing a beam with no frequency shift. In this way we can still use our AOM as a shutter even if we don't want to modulate the frequency of our beam. The set-up of these AOM tracks, along with one used for absorption imaging, is seen in Figure 2.9.

2.3 MOT Characterization via Absorption Imaging

Absorption imaging is a relatively simple way to characterize the number of atoms and temperature of the atoms in our MOT. If a laser is on resonance with a cloud of atoms, when it passes through some light will be absorbed and then scattered in a random direction. If the beam is larger than the cloud of atoms, then only some area of it will be absorbed. Imaging this beam on a camera, this absorption creates a shadow on the beam, contrasted by the light that passes through the atoms without absorption (see Figure 2.10).

From the contrast we can obtain the atom number, while the expansion of this shadow over time, after releasing the cloud, can tell us the temperature. For both measurements, we used the same setup, see Figure 2.11, of a beam on resonance with the $F = 2$ to $F' = 3$

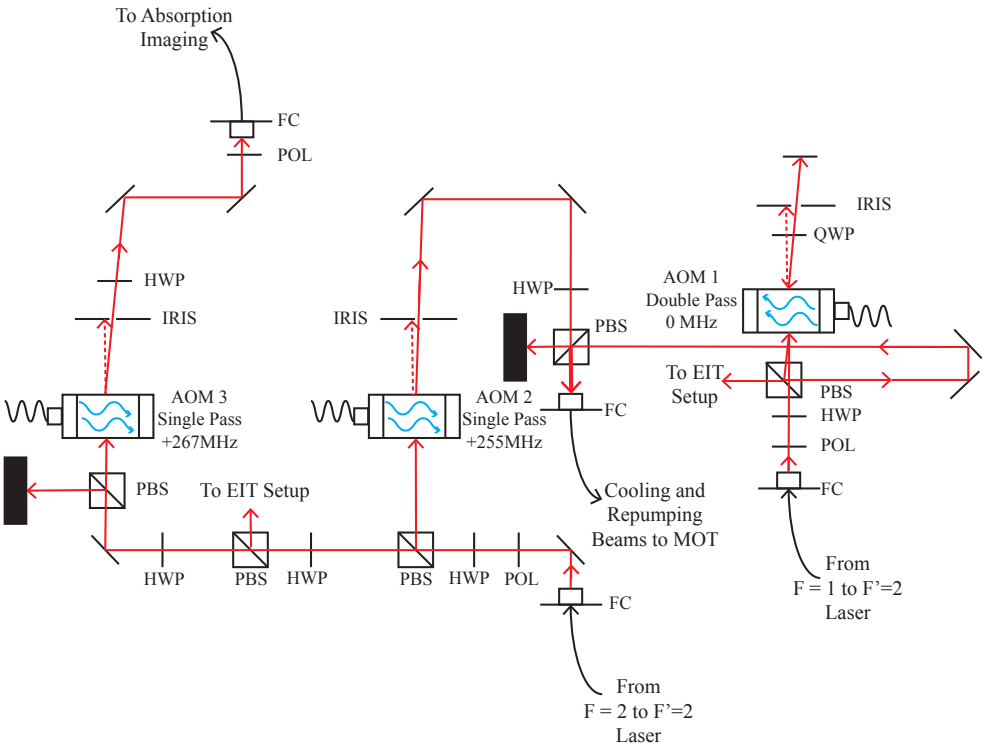

Figure 2.9: The F=1 to F'=2 laser is passed through AOM1 in a double-pass, no frequency shift configuration. This is our repumping laser. The F=2 to F'=2 laser undergoes a single pass, +255 MHz shift through AOM1. This serves as our red-detuned cooling laser. It is coupled to the same fiber coupler as the repumping laser. These two beams are then put into the cooling laser system seen in figure (2.3). Using polarizing beamsplitters to create additional beam pathways, the F=2 to F'=2 laser can passed through another single-pass plus configuration. This time the shift is 267 MHz through AOM3, which is exactly on resonance with the F=2 to F'=3 transition, serving as our absorption imaging beam

.

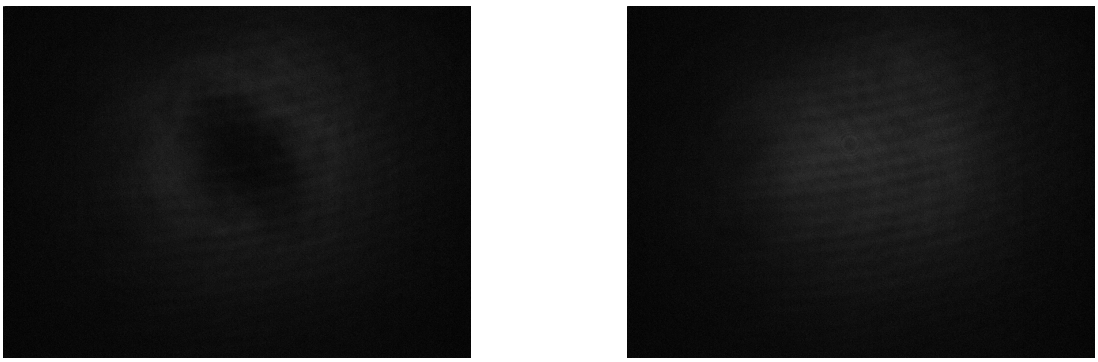

(a) Camera image of beam with absorption. (b) Camera image of beam at full transmission

Figure 2.10: Shadow produced by absorption of beam by atomic cloud compared with full transmission of beam.

transition (obtained through the set up in Figure 2.9). We then expanded and collimated these beam using a Galilean telescope set-up, such that the beam was larger than the cloud of atoms. Placing a camera after the beam passes through the MOT we image the effects of absorption on our laser beam.

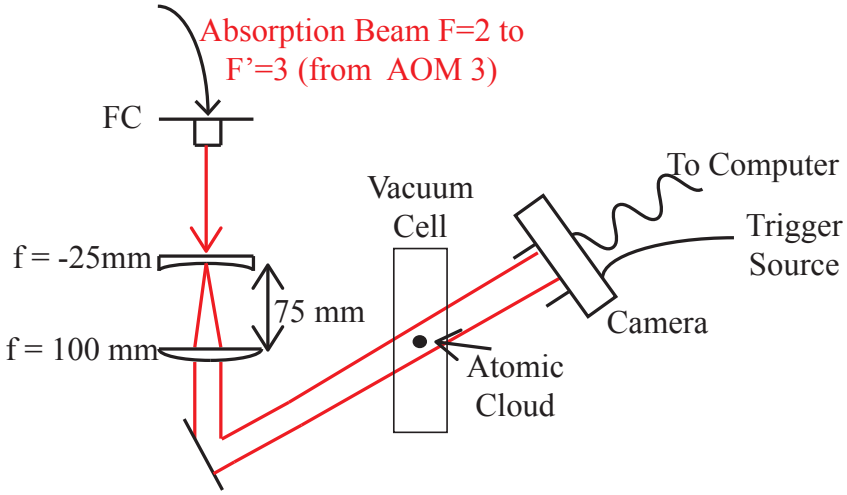

Figure 2.11: Using a combination of a plano-concave and plano-convex lens we expand and collimate our beam to absorption image our cloud of atoms

.

2.3.1 Number of Atoms

If our absorption probe is below saturation intensity of the Rubidium D2 transition ($\approx 3\text{mW/cm}^2$) [9], its intensity after absorption can be determined from

$$I(\omega) = I_o e^{-\frac{\text{O.D. } \Gamma^2}{4(\omega-\omega_o)^2+\Gamma^2}}, \tag{2.16}$$

where ω is our probe frequency, ω_o is resonance frequency, I_o is the initial intensity of our beam, Γ is the linewidth of the excited state, and O.D. is the optical density [12]. Tuning our absorption beam to resonance gives

$$\ln\left(\frac{I(\omega)}{I_o}\right) = -\text{O.D.} \tag{2.17}$$

We can also determine this absorption change using Beer's law

$$\frac{dI}{dZ} = -\sigma_o \rho I, \tag{2.18}$$

where $\sigma_o = \frac{3\lambda^2}{2\pi}$ is the atomic cross section on resonance for a two-level atom [12], and ρ the

atomic density. Integrating this equation leads to

$$I = I_o e^{-\sigma_o n} \tag{2.19}$$

where $n = \int_{-\infty}^{\infty} \rho(x, y, z) dz$ is the differential column density of atoms in the z-direction for a specific point in the xy plane [15]. From these two equations we see that

$$n = \frac{\text{O.D}}{\sigma_o} \tag{2.20}$$

Since pixels on a camera are of finite size, we cannot use this infinitesimal formulation. However, assuming that atomic column density and optical depth is constant over the area of one pixel, the number of atoms in this pixel is $N_{atom/pix} = n_{pix} A_{pix}$, where n_{pix} is the atomic column density of that one pixel and A_{pixel} is the area. Using a sum we can than determine the total number of atoms as

$$N_{atoms} = \sum_{\text{all pixels}} n_{pix} A_{pix} = \frac{A_{pix}}{\sigma_o} \sum_{\text{all pixels}} \text{O.D}_{pix}. \tag{2.21}$$

Both A_{pix} and σ_o are constants. We just need to calculate $O.D._{pix} = -\ln\left(\frac{I(\omega)}{I_o}\right)_{pix}$. This reduces to finding the intensity of each pixel during absorption of the beam and during full transmission when no atoms are present. In our case, the camera records each image in grayscale. In this scale, each pixel carries intensity information through an assigned value, with higher values corresponding to higher relative intensities. Therefore, experimentally, the number of atoms can be calculated by

$$N_{atoms} = \frac{-A_{pix}}{\sigma_o} \sum_{i,j} \ln\left(\frac{\text{Im}_{i,j}^{abs} - \text{Im}_{i,j}^{back}}{\text{Im}_{i,j}^{trans} - \text{Im}_{i,j}^{back}}\right), \tag{2.22}$$

where i, j represent each different pixel, and Im^{abs}, Im^{trans}, Im^{back} the camera images representing beam power during absorption, during transmission, and the background light, respectively [14].

The pulse sequence we used to obtain these images was a simple one (see Figure 2.12). We left the absorption beam continuously on, and trigger the camera, with a shutter speed of 0.016 ms, to record an image as we turned off the trapping coils and cooling beams
Through this sequence we can obtain the images like the one above in Figure 2.10. Taking a transmission and background image, which can be done manually, we can then use the equation above to create a relative optical depth profile of our atomic cloud (see Figure 2.13).

To increase the number of atoms in our MOT we can turn on our rubidium source, also

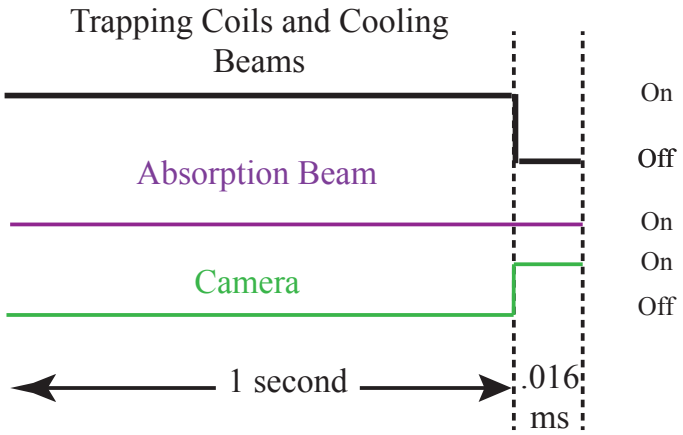

Figure 2.12: We load our MOT for 1 second. At this point we shut off the trapping coils and cooling/repumping beams and record a camera image

.

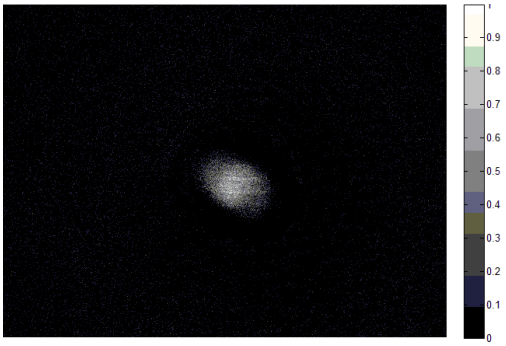

(a) Density Image of MOT

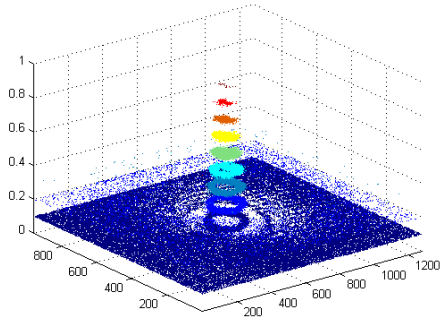

(b) Contour diagram of Relative Atomic Density

Figure 2.13: Optical Depth Profile of our Atomic Cloud. The 0-1 scale for each image corresponds to the relative intensity of the shadow produced by absorption at that point. The darkest spot would correspond to 1.0. The colors have been inverted for visualization. The x-y axes on (b) correspond to pixel(i,j). Each pixel is 3.75 μm in width and height

known as a dispenser or oven. This consists of Rubidium Chromate, which releases rubidium vapor when a current passes through it. We can adjust the current from 0-6 Amps. We were interested in how much we could increase the number of atoms by turning on the dispenser. This measurement took images every 30 seconds for 15 minutes of the rubidium dispenser being turned on. Although it could have been kept on longer, we have experienced issues possibly related to excessive rubidium in our system that prevented a longer duration. We see that over the span of 15 minutes the rubidium atoms in our trapped atomic ensemble increased from 13 million to 20 million atoms (see Figure 2.14).

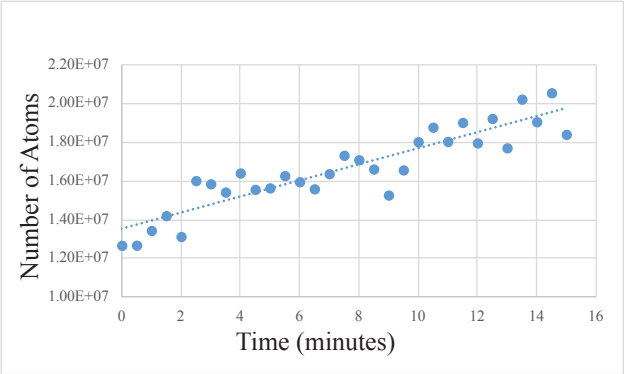

Figure 2.14: We can nearly double our atomic number by turning on a rubidium dispenser that increases the number of atoms linearly over time.

From Figure 2.13b the size of the trapped atomic cloud can be determined. For Figure 2.13b, the cloud has a diameter of approximately 200 pixels, corresponding to 0.75 mm. For this trial the number of atoms was 10^7. Assuming the MOT is approximately spherical this corresponds to an atom number density of

$$\rho_{\text{atoms}} = \frac{\text{Number of Atoms}}{\text{Volume of Cloud}} = \frac{10^7}{\frac{4}{3}\pi\,(0.375mm)^3} \approx 4.5 \times 10^7 \frac{\text{atoms}}{\text{mm}^3}. \tag{2.23}$$

This thesis is working towards enveloping this atomic cloud of cold rubidium atoms within an optical cavity (see Figure 2.15). The cavity mode at the center of this cavity will have a width of approximately 0.1 mm. Aligning the light in the cavity to hit the center of the atoms, we can approximate this mode as selecting a cylinder of the atomic cloud. The cylinder's radius is half of the cavity mode's width at the center, and the height is the diameter of the atomic cloud. Therefore, the cavity mode encompasses a number of atoms determined by

$$N_{\text{CavAtoms}} = \rho_{\text{atoms}} V_{\text{CavMode}} \approx \left(4.5 \times 10^7 \frac{\text{atoms}}{\text{mm}^3}\right)\left(\pi[0.05\text{mm}]^2[0.75\text{mm}]\right) \approx 2.7 \times 10^5 \text{atoms}. \tag{2.24}$$

Compared to a similar experimental setup where 3×10^4 atoms were coupled in the atomic-cavity ensemble, our result suggest we could possible couple an order of magnitude larger number of atoms [17]. Based on this result we believe our cold rubidium cloud is dense enough to move forward with coupling to an optical cavity.

2.3.2 Temperature

Turning off the trapping coils and cooling/repumping beams, the atoms previously contained in the MOT undergo thermal expansion. On our camera, this corresponds to the

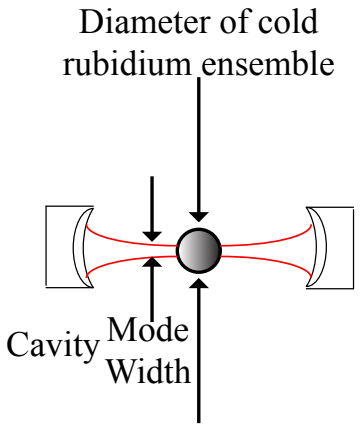

Figure 2.15: Coupling the atomic ensemble to a cavity. The outlook of this thesis includes constructing a cavity around the atoms to increase light-matter interaction. We estimate our cavity mode with will be 0.1 mm at the center, thus selecting a specific volume of our atomic cloud

.

shadow on our beam expanding. This expansion is Gaussian and the density of the atomic cloud can be expressed as

$$n(x_i,t) = \frac{1}{\sqrt{2\pi}\sqrt{\sigma_{x_i,0}^2 + \frac{k_B T_{x_i}}{m}t^2}} \exp\left[-\frac{x_i^2}{2\left(\sigma_{x_i,0}^2 + \frac{k_B T_{x_i}}{m}t^2\right)}\right], \tag{2.25}$$

where $\sigma_{x_i,0}$ is the $1/\sqrt{e}$ width of our atomic cloud at $t = 0$, m the mass of a single rubidium atom, k_B is Boltzmann's constant, and T_{x_i} is the temperature of the atoms along the direction of the absorption beam [14]. For perfectly balanced optical molasses beams, the trapped atomic cloud should be spherical and the temperature uniform in all directions. However, as seen by Figure 2.17, the cold atomic cloud is not spherical, suggesting an imbalance of the cooling beams and thus differing temperatures along the direction of each cooling beam. Focusing on the exponential of of Equation 2.25 we see that the $1/\sqrt{e}$ Gaussian width of our atomic cloud is

$$\sigma_{x_i}(t) = \sqrt{\sigma_{x_i,0}^2 + \frac{k_B T_{x_i}}{m}t^2}. \tag{2.26}$$

Taking a sequence of images over time, we can fit their $1/\sqrt{e}$ Gaussian width to this function to determine the temperature in the direction of the absorption imaging beam.

The pulse sequence in Figure 2.16 was used to image the atomic cloud's expansion. Ideally, all 9 images should be taken consecutively. However, the camera could not trigger fast enough for our 500μs intervals. Therefore, we had to wait for the atoms to reload in

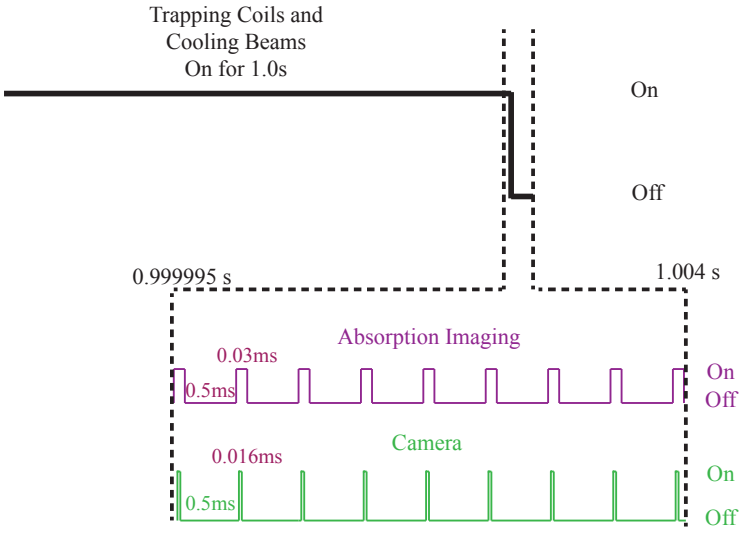

Figure 2.16: We load our MOT for 1 second. At this point we shut off the trapping coils and cooling/repumping beams. At this point, we pulse our absorption beam for 30 μs and trigger our camera to record an image 5μs after each the beginning of absorption pulse.Each pulse is separated by 500μs, covering a total expansion time of 4 ms. The shutter speed of the camera was 16μs

.

the MOT before we captured our next image. To compensate for this we captured several images for each of the 9 pulse times, and then averaged these images. The results for a trial following this pulse sequence are below in Figure 2.17 :

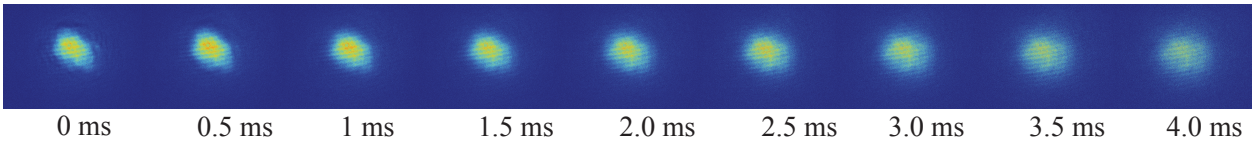

Figure 2.17: The expansion of the atomic cloud for pulsed absorption imaging.

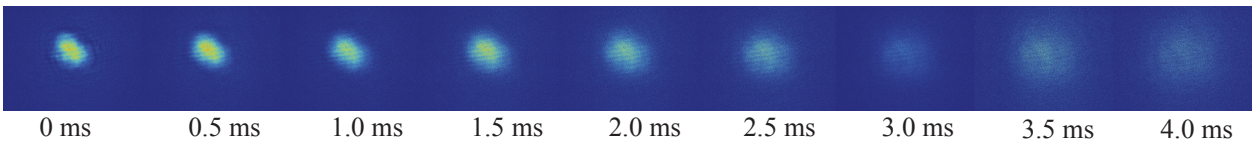

Figure 2.18: The expansion of the atomic cloud for continuous absorption imaging.

Directly after this trial was taken, the same measurement was performed, but this time with a continuous absorption signal (see Figure 2.18). The goal of this measurement was to understand how the absorption probe affected the atoms. As we see in figures Figure 2.17 and Figure 2.18, the atomic cloud diffuses more quickly with a continuous absorption beam.

This suggests that the atoms warm up faster as a result of the continuous absorption probe. Indeed, fitting our data to the theoretical expansion we measured $540\mu K$ for the pulsed trial whereas for the continuous absorption trial we measured 2.2 mK. The theoretical curve versus our data for both trial are included below in Figure 2.19 and Figure 2.20.

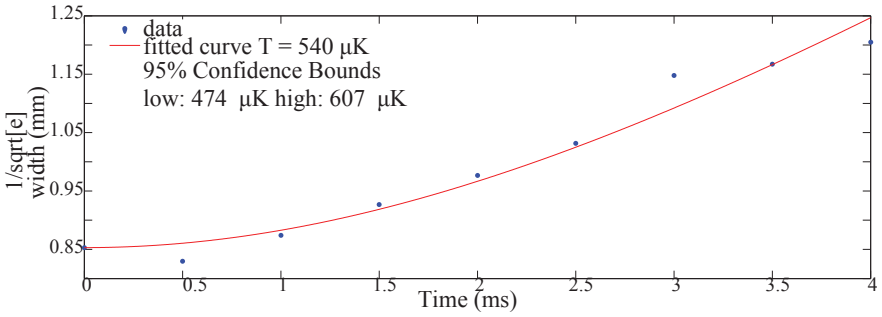

Figure 2.19: Fitting Equation (2.26) to determine temperature for pulsed absorption imaging

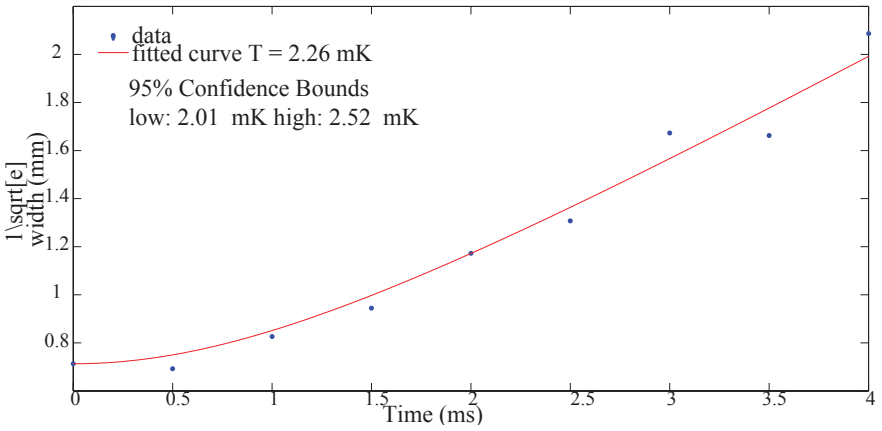

Figure 2.20: Fitting Equation (2.26) to determine temperature for continuous absorption imaging

The doppler cooling limit of the D2 line of Rubidium is 145.6 μK [9]. Our pulsed results give 500 μK. However, as suggested by the differing temperatures obtained through pulsed and continuous absorption imaging, the absorption beam is heating the atomic cloud. To obtain an unbiased temperature measurement it could be beneficial to use a technique that interacts less with the atomic cloud. This should give us a truer temperature measurement. A description of alternate techniques to measure temperature and lower the temperature can be found in [14]. Of most importance to this thesis is not how cold we can cool our atoms, but if their temperature is low enough to coherently control our atoms in an optical cavity. This will be discussed in the following chapter.

Chapter 3

Electromagnetically-Induced Transparency

The previous chapter focused on creating a light-atom interface. Using lasers we were able to control the motion of atoms and trap them with the assistance of a magnetic field. Light was also used to characterize the atoms through absorption. These experimental tools relied purely on light-atom interactions. To construct a quantum phase gate where one light field modifies another we need light-atom-light interactions. That is, since light cannot directly manipulate light, we need to mediate the interaction of two light fields with atoms. Electromagnetically Induced Transparency (EIT) is the tool we will use to control light-atom-light interactions.

In 1990, Harris showed that laser induced coherence of atomic systems in a 3-level Λ configuration (see Figure 3.1) could be used to modify the optical response of the medium by causing quantum interference between the excitation pathways in the system. This coherence could be accomplished with a strong control laser and much weaker probe laser. Under the right resonance conditions of both lasers, the linear susceptibility of the medium with respect to the probe laser can be eliminated. This eliminates the absorption and refraction experienced by this beam, hence the medium appears transparent. The utility of EIT is that it allows the coherent optical control of a medium. Therefore, one laser can alter how another laser interacts with the medium. This not only gives us light-atom-light interactions, but a method of manipulating the resultant effects. In fact, this control offered by EIT was what enabled the first storage and retrieval of optical qubits by [7] mentioned in the introduction of Chapter 2. Light cannot be stopped, and hence stored, without EIT, making it a tool that can be used to create optical quantum memories [20].

Besides its usefulness for quantum memories, EIT is also able to manipulate the light induced phase shifts we desire for a quantum logic gate. As will be discussed in Chapter 4, this

is accomplished through EIT's affect on the nonlinear susceptibility of an atomic medium. As with using cold-atoms for our light-atom interface, the use of EIT to mediate light-atom-light interactions builds upon a strong foundation of research in quantum information science. We plan to combine EIT in a unique way with optical cavities to create a two-qubit optical phase gate, adding novel science to this field.

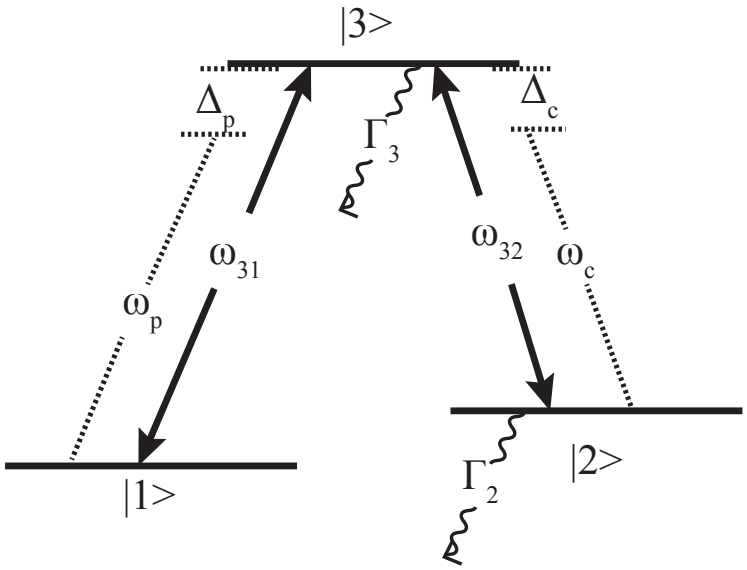

Figure 3.1: An EIT Lambda, Λ, system consists of a ground state $|1\rangle$, a metastable state $|2\rangle$, and excited state $|3\rangle$. The ground and metastable state do not have a dipole allowed transition, resulting in a very small decay rate, Γ_2, hence the name metastable. However, both these states have dipole allowed transitions to the excited state. The $|1\rangle \rightarrow |3\rangle$ transition has resonance frequency ω_{31} and the $|2\rangle \rightarrow |3\rangle$ transition has resonance frequency ω_{32}. The probe laser addresses the former transition and has detuning $\Delta_p = \omega_p - \omega_{31}$, while the control laser addresses the latter transition and has detuning $\Delta_c = \omega_c - \omega_{32}$.

3.1 Theoretical Treatment

3.1.1 Deriving the EIT Hamiltonian

Electromagnetically Induced Transparency occurs in three-level atoms, the most common use is in the Λ configuration seen in Figure 3.1. The Hamiltonian of this system can be written as

$$H = H_o + H_1, \tag{3.1}$$

where H_o describes the atomic system with no external fields, and H_1 accounts for pertur-

bation from these applied fields. In our case, the applied fields that interact with our atoms are the electric fields of the probe and control lasers shown in Figure 3.1.

For a single atom, it is easy to construct H_o as it can only exist in one of the three possible states $|1\rangle, |2\rangle, |3\rangle$:

$$H_o = \left(\sum_n |n\rangle \langle n|\right) H_o \left(\sum_n |n\rangle \langle n|\right) = \begin{bmatrix} \hbar\omega_1 & 0 & 0 \\ 0 & \hbar\omega_2 & 0 \\ 0 & 0 & \hbar\omega_3 \end{bmatrix}. \tag{3.2}$$

It is not as easy to find the perturbing Hamiltonian, caused by the electric field of both the probe and control lasers:

$$\boldsymbol{E} = \boldsymbol{\mathcal{E}_p} \cos(\omega_p t - \boldsymbol{k_p} \cdot \boldsymbol{r}) + \boldsymbol{\mathcal{E}_c} \cos(\omega_c t - \boldsymbol{k_c} \cdot \boldsymbol{r}). \tag{3.3}$$

However, the wavelength of our light, $7.8 * 10^{-7}$m, is three orders of magnitude larger than the Bohr Radius of approximately 10^{-10}m. Using the trigonometric identity

$$\cos(\omega t - \boldsymbol{k} \cdot \boldsymbol{r}) = \cos(\omega t)\cos(-\boldsymbol{k} \cdot \boldsymbol{r}) - \sin(\omega t)\sin(-\boldsymbol{k} \cdot \boldsymbol{r}), \tag{3.4}$$

we can rewrite the electric field as

$$\boldsymbol{E} = \boldsymbol{\mathcal{E}_p} \cos(\omega_p t) + \boldsymbol{\mathcal{E}_c} \cos(\omega_c t), \tag{3.5}$$

since $\boldsymbol{k} \cdot \boldsymbol{r} \ll 1$. This is known as the Dipole Approximation, as it assumes the charge separation of the dipole (in our case the size of the atom) to be much smaller than the wavelength of light [21].

Assuming the dipole is aligned with the electric field, we can write the perturbing Hamiltonian as

$$H_1 = -qE\hat{r}, \tag{3.6}$$

where q is the charge of our dipole and r the separation. Defining the dipole moment operator $\mu = qr$, where $\mu_{nm} = \mu^*_{mn} = \langle n|\mu|m\rangle$, we can write H_1 in the same eigenbasis as H_o as

$$H_1 = -\mu E = -E \left(\sum_n |n\rangle \langle n|\right) H_1 \left(\sum_n |n\rangle \langle n|\right) = -\begin{bmatrix} 0 & 0 & \mu_{13} \\ 0 & 0 & \mu_{23} \\ \mu_{31} & \mu_{32} & 0 \end{bmatrix} E. \tag{3.7}$$

The absence of μ_{12} and μ_{21} assumes that they are dipole forbidden transitions. The absence

of the diagonal elements assumes that the atoms have no permanent dipole moments.

Although it may look relatively simple, the Hamiltonian in this form still doesn't physically illuminate what is happening. We can get closer to a more intuitive Hamiltonian by transforming to the interaction picture. As the operator for this transformation is $U = e^{iH_o t/\hbar}$, we only need to consider how H_1 changes in this picture since U and H_o commute. Applying this operator to H_1 we get:

$$UH_1U^\dagger = -E \begin{bmatrix} 0 & 0 & \mu_{13}e^{i(\omega_1-\omega_3)t} \\ 0 & 0 & \mu_{23}e^{i(\omega_2-\omega_3)t} \\ \mu_{31}e^{i(\omega_3-\omega_1)t} & \mu_{32}e^{i(\omega_3-\omega_2)t} & 0 \end{bmatrix}. \tag{3.8}$$

Writing the electric field in terms of exponentials

$$E = \frac{\mathcal{E}_p}{2}\left(e^{i\omega_p t} + e^{-i\omega_p t}\right) + \frac{\mathcal{E}_c}{2}\left(e^{i\omega_c t} + e^{-i\omega_c t}\right), \tag{3.9}$$

we see that each of the four non-zero matrix elements in (3.8) consists of several exponential terms with various sums of ω_p, ω_c, ω_1, ω_2, and ω_3. We can get rid of many several of these terms using the Rotating Wave Approximation. This approximation assumes that any rapidly oscillating term will average out to zero over the span of observation. For example, ω_c is near the transition frequency $\omega_{21} = \omega_2 - \omega_1$; therefore, $\omega_c - \omega_{21} \ll \omega_c + \omega_{21}$. This allows us to get rid of any terms with $\omega_c + \omega_2 - \omega_1$. Following similar logic, several other terms can also be neglected as they oscillate much more rapidly than the terms we are keeping [21]. This reduces the H_1 in the interaction picture to

$$UH_1U^\dagger = -\frac{1}{2} \begin{bmatrix} 0 & 0 & \mathcal{E}_p\mu_{13}e^{i(\omega_1-\omega_3+\omega_p)t} \\ 0 & 0 & \mathcal{E}_c\mu_{23}e^{i(\omega_2-\omega_3+\omega_c)t} \\ \mathcal{E}_p\mu_{31}e^{i(\omega_3-\omega_1-\omega p)t} & \mathcal{E}_c\mu_{32}e^{i(\omega_3-\omega_2-\omega_c)t} & 0 \end{bmatrix}. \tag{3.10}$$

Defining the Rabi frequencies as

$$\Omega_p = \mathcal{E}_p|\mu_{13}|/\hbar \tag{3.11}$$

$$\Omega_c = \mathcal{E}_c|\mu_{13}|/\hbar \tag{3.12}$$

we can return to the Schrodinger picture and add our new form of H_1 with H_o to get

$$H_{EIT} = \frac{\hbar}{2}\begin{bmatrix} 2\omega_1 & 0 & \Omega_p e^{i\phi_p} e^{i\omega_p t} \\ 0 & 2\omega_c & \Omega_c e^{i\phi_c} e^{i\omega_c t} \\ -\Omega_p e^{-i\phi_p} e^{-i\omega_p t} & -\Omega_c e^{-i\phi_c} e^{-i\omega_c t} & 2\omega_3 \end{bmatrix}. \tag{3.13}$$

Applying one further approximation the time dependence can be removed, along with the dipole phase $e^{i\phi_p}$ or $e^{i\phi_c}$ not included in the Rabi frequency definitions as we only took the magnitude of the dipole operators. This approximation defines the Hamiltonian in a co-rotating basis with the operation

$$\tilde{U}(t) = \begin{bmatrix} -e^{-i\omega_p t} e^{-i\phi_p} & 0 & 0 \\ 0 & e^{-i\omega_c t} e^{-i\phi_c} & 0 \\ 0 & 0 & 1 \end{bmatrix}, \tag{3.14}$$

with the relationship to the previous space $|\tilde{\psi}\rangle = \tilde{U}(t)\,|\psi\rangle$. Upon substitution into the Schrodinger equation, it can be shown that for the Hamiltonian to satisfy the Schrodinger equation in this new wave space, then

$$\tilde{H}_{EIT} = i\hbar \frac{\partial \tilde{U}}{\partial t}\tilde{U}^{\dagger} + \tilde{U} H_{EIT} \tilde{U}^{\dagger}. \tag{3.15}$$

This allows us to write our Hamiltonian in this space as

$$\tilde{H}_{EIT} = \frac{\hbar}{2}\begin{bmatrix} 2(\omega_1 + \omega_p) & 0 & -\Omega_p \\ 0 & 2(\omega_2 + \omega_c) & -\Omega_c \\ -\Omega_p & -\Omega_c & 2\omega_3 \end{bmatrix}. \tag{3.16}$$

Adding the constant $-2(\omega_1 + \omega_p)$, which has no physical effect since we are only concerned with energy differences between levels, gives the final and most commonly found form of the EIT Hamiltonian as

$$\tilde{H}_{EIT} = -\frac{\hbar}{2}\begin{bmatrix} 0 & 0 & \Omega_p \\ 0 & 2(\Delta_p - \Delta_c) & \Omega_c \\ \Omega_p & \Omega c & 2\Delta_p \end{bmatrix}, \tag{3.17}$$

where $\Delta_p = \omega_p - \omega_3 + \omega_1$ and $\Delta_c = \omega_c - \omega_3 + \omega_2$ are the single-photon detunings (note, for laser cooling we defined the detuning with δ, for EIT we will use Δ) [21].

3.1.2 Dark States, Linear Susceptibility, and Slow Light

Here we will briefly present some of the important properties derivable from this EIT Hamiltonian.

Dark States

Following [20], the eigenstates of the EIT Hamiltonian can be expressed in terms of the mixing angles

$$\tan(\theta) = \frac{\Omega_p}{\Omega_c} \tag{3.18}$$

$$\tan(2\phi) = \frac{\sqrt{\Omega_p^2 + \Omega_c^2}}{\Delta}. \tag{3.19}$$

Using these definitions, the three eigenstates can succinctly be written as:

$$\begin{aligned} |a^+\rangle &= \sin\theta \sin\phi \,|1\rangle + \cos\phi \,|3\rangle + \cos\theta \sin\phi \,|2\rangle \\ |a^o\rangle &= \cos\theta \,|1\rangle - \sin\theta \,|2\rangle \\ |a^-\rangle &= \sin\theta \cos\phi \,|1\rangle - \sin\phi \,|3\rangle + \cos\theta \cos\phi \,|2\rangle \,, \end{aligned} \tag{3.20}$$

where the +,0,- represents an increase, no change, and decrease in energy from the bare atom states, respectively. Of interest here is $|a^o\rangle$, also know as the dark state. This name stems from $|a^o\rangle$ having no component of the excited state $|3\rangle$. Therefore, an atom formed in $|a^o\rangle$ has no possibility of excitation to $|3\rangle$. With no excitation to the excited state of the lambda system, there can be no emission, hence the atom will remain "dark." Preparing an atom in this state can be done with a weak probe $\Omega_p \ll \Omega_c$, as this causes $\sin\theta \to 0$ and $\cos\theta \to 1$, making the ground state equivalent to the dark state, $|a^o\rangle = |1\rangle$.

Linear Susceptibility

We have stated that EIT drastically modifies the optical properties of our medium. One example of this is apparent through the effects on dispersion and absorption of the probe laser. To first order, these properties are described by the linear susceptibility, χ, which is described by

$$\boldsymbol{P} = \epsilon_o \chi \boldsymbol{E} \tag{3.21}$$

where $\boldsymbol{P}$ is the dielectric polarization of the medium, $\boldsymbol{E}$ the electric field, and ϵ_o the permittivity of free space. Absorption of the laser is described by the imaginary component of χ and dispersion by the real component.

Although it won't be shown here, a detailed derivation can be found in [21], the linear susceptibility for EIT can be found by transforming our Hamiltonian from one that describes single atom wave functions to one that describes the atomic population of each state with density operators. Once these density operators are found in the same corotating basis, the

relation $\boldsymbol{P} = \mathrm{Tr}(\rho\mu)$ can be used to write the polarization in terms of our density operators ρ and already derived dipole operators. Setting this definition of polarization to the previous in 3.21, the linear susceptibility can be shown to be:

$$\chi = \frac{2N|\mu_{13}|\Omega_p}{\mathcal{E}_p\epsilon_o}\frac{-2\left(\Gamma_{12} + i\left(\Delta_c - \Delta_p\right)\right)\Omega_p}{4\left(\Gamma_{13} - i\Delta_P\right)\left(i\Gamma_{12} - \Delta_c + \Delta_p\right) + i\Omega_c^2}. \tag{3.22}$$

Plotting the imaginary and real parts of this susceptibility as a function of the two photon-detuning, $\Delta_p - \Delta_c$, the absorption and dispersion of an EIT spectrum take the form in Figure 3.2:

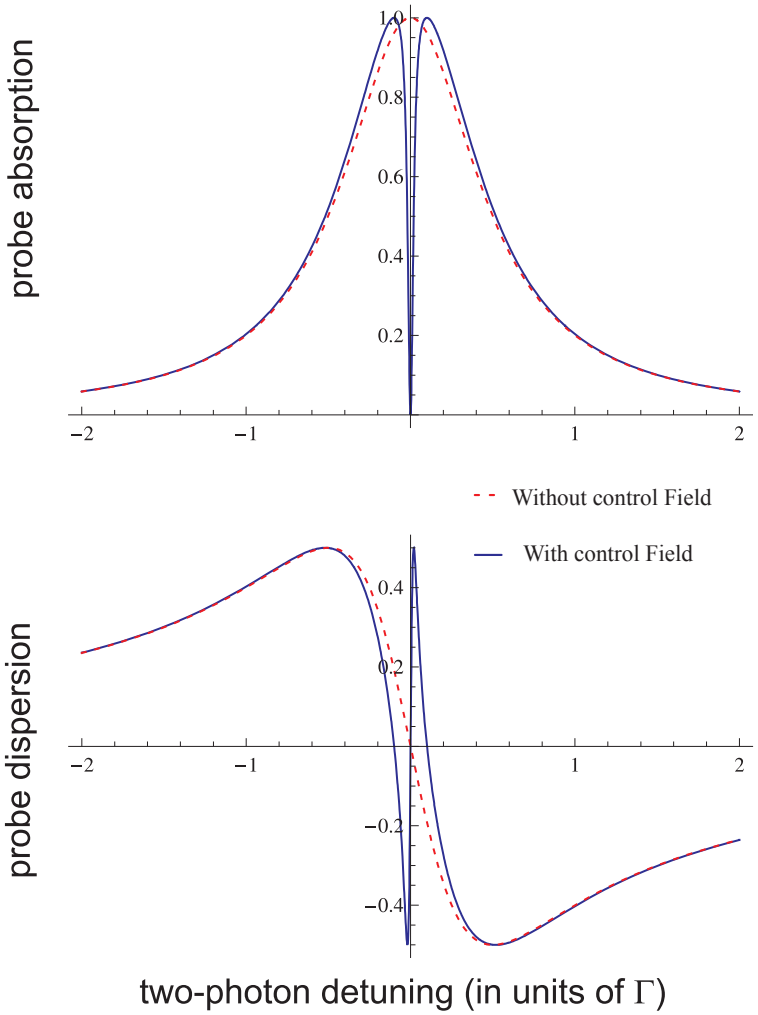

Figure 3.2: Absorption and Dispersion of EIT probe laser (blue curves) overlayed with characteristic curves without repumping control laser (dashed red). The y-axis for absorption corresponds to $\mathrm{Im}[\chi]$ and for dispersion $\mathrm{Re}[\chi]$, for Equation 3.22 normalized to one. In units of Γ the two-photon detuning is $\Delta = \frac{\Delta_p - \Delta_c}{\Gamma_{13}}$. The relationship between the Rabi frequencies is $\Omega_c = 100\Omega_p$

.

From the top graph in Figure 3.2 we see the characteristic transparency peak of EIT as absorption goes to zero for two-photon detuning equal to zero. The dispersion curve experiences a drastic change in slope near two-photon detuning. This is responsible for a very remarkable effect of EIT.

Slow Light

The the group velocity of our probe laser can be written as:

$$v_{gr} = \frac{c}{n + \omega_p(dn/d\omega_p)}, \tag{3.23}$$

where $n = \sqrt{1 + \mathrm{Re}[\chi]}$ is the refractive index, $dn/d\omega_p$ the linear dispersion, and c the speed of light [22]. From our dispersion curve above, we see that near two-photon detuning the dispersion deviates from its classical negative slope and increases quite rapidly. This creates a large positive value for $dn/d\omega_p$. Since this is in the denominator of our group velocity equation, this results in a reduction of our probe laser's group velocity. Using this technique has led to group velocities less than 20m/s and even stopping, and hence storage, of light[20]!

3.2 EIT Implementation

As with laser cooling, EIT requires a specific atomic level scheme. EIT requires a three level Λ atom system. We can engineer this once again through the use of AOMs and the hyperfine levels of the rubidium atoms.

3.2.1 Lambda System

From our theoretical Λ system in Figure 3.1, we see that we need a ground state and metastable state, both with pathways to the same excited state, but with no pathways between each other. Reexamining the hyperfine transitions of Rb^{87}, (see Figure 3.3), we can construct this level scheme.
As seen in Figure 3.3, F=1 is the ground state, and so the F=1 to F'=1 transition will be addressed with our probe laser. Slightly higher in energy, F=2, will serve as the metastable state since its decay rate to F=1 is very slow. The control laser will address this F=2 to F'=1 transition.

3.2.2 AOM Setup

As we saw in the theory, the EIT Dark State relies on very specific detuning conditions

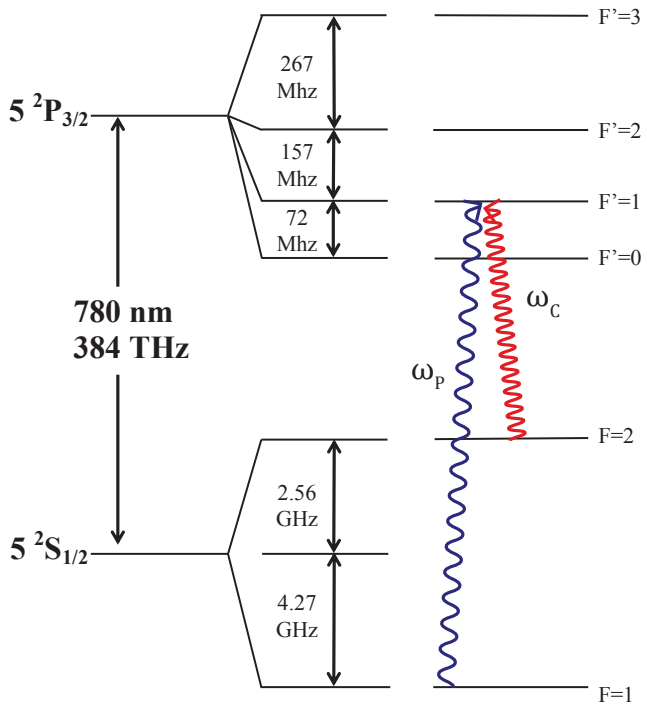

Figure 3.3: Exciting atoms from the F=1 to F'=1, they can only decay to F=1 or F=2. Therefore, we can continually repump atoms back into the F'=1 state if we have another beam addressing the F=2 to F'=1 transition.

.

of both the control and probe lasers. As before, we can control our frequencies through the use of AOMs. However, if we want to quickly and easily observe the effect of our lasers for different detunings, we cannot use a single-pass AOM setup. As explained in Chapter 2, every time the frequency is changed on a single-pass AOM, the angle of the diffracted beam moves, and coupling to the fiber is lost. However, by passing our laser through the AOM twice, we can overcome this (Figure 3.4).

As we see in Figure 3.4, if we use a double-pass, double-frequency configuration, our final beam will come out in the same direction for any frequency shift. This allows us to easily scan the frequency of our probe and control lasers, which is necessary to create EIT [18].

3.3 Measurements

3.3.1 Absorption

Before attempting to see EIT with our lambda system, we wanted to optimize the alignment of the F=1 to F'=1 probe beam as it passed through the atomic ensemble (see Figure 3.6) by maximizing its absorption. However, without the F=2 to F'=1, the atoms will

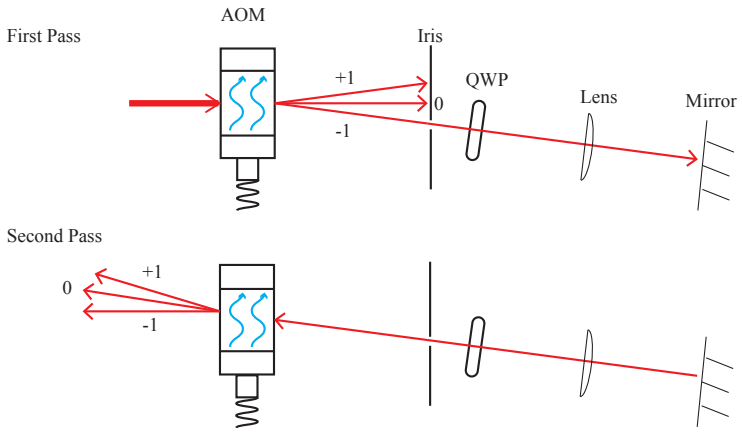

Figure 3.4: The sign of the frequency shift depends on the propagation direction of the laser. Therefore, to obtain a double frequency shift configuration,the diffraction mode of each beam will be in opposite directions, resulting in no angular beam displacement. A lens is used to guide the returning beam to the same point in the AOM as the original

.

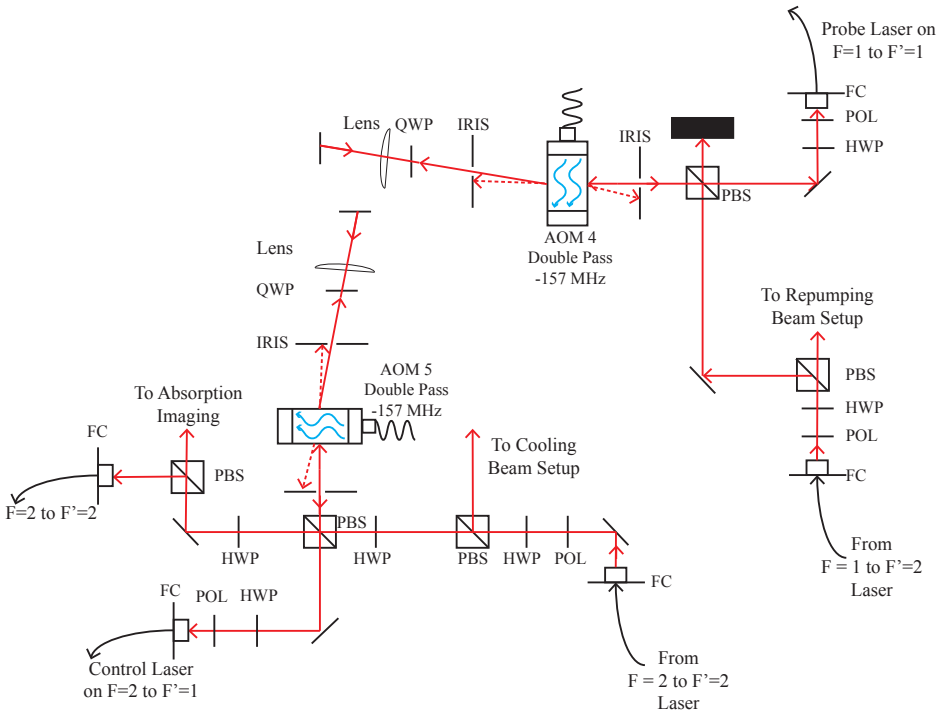

Figure 3.5: From figure 2.9, there were beam paths directed to EIT setup. Here are the AOM setups these beams encounter. From the F'=1 to F=2 laser, a double pass, -157 MHz frequency is set up with AOM 4. This creates our probe laser addressing the F=1 to F'=2 laser. From the F'=2 to F=2 laser, another double-pass, -157 MHz is set up with AOM5. This creates our control laser addressing the F=2 to F'=1 transition.

build up in the F=2 state, resulting in very little absorption on the F=1 to F'=1 probe laser.

We can avoid this by addressing the F=2 to F'=2. This transition does not create a lambda system, so we aren't working with EIT. As seen in the Figure 3.5, we have a beam path already at this transition, so there was no need to construct any more AOM pathways.

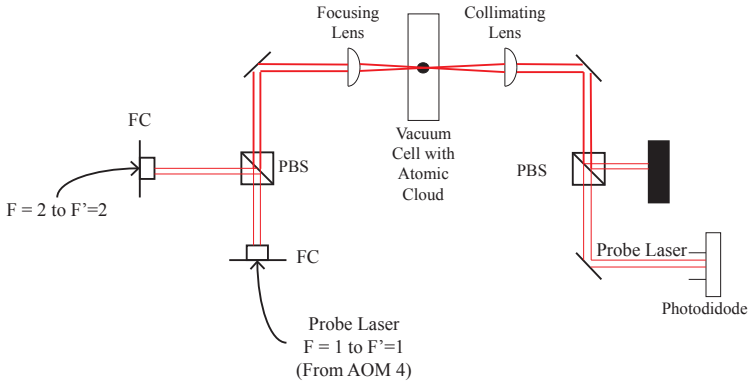

Figure 3.6: We coalign our probe and F=2 to F'=2 beams using a PBS. The coaligned beams are then passed through the MOT, using an adjustable focusing lens to optimize alignment. Afterwards, another lens is used to collimate the beams. Following this, a PBS is used to separate the two beams, allowing the probe to end its journey at a photodiode connected to an oscilloscope

.

Absorption imaging utilized the shadow a cloud of atoms creates in a laser beam on resonance. We again utilize the same principle. If our atoms are on resonance with our probe beam, then some of the light will be absorbed, resulting in a smaller beam power upon exiting the atomic cloud. The setup we used for this is in Figure 3.6. Since we are not concerned with the size of the MOT, but only maximizing absorption, we tightly focus our beams to precisely hit the most atomically dense region of our atomic cloud.

Triggering our oscilloscope to the quantum composer signal that shuts off our trapping coils and cooling/repumping beams (for pulse sequence see Figure 3.7), we should then expect to see a drop in voltage of our probe signal at this is point. This is because the probe beam is addressing the natural transition frequency of F=1 to F'=1. With the MOT on, the trapping coils and cooling/repumping beams cause Zeeman splitting and an AC Stark shift moving this transition away from its natural frequency. Therefore, when the MOT is turned off, the probe beam will be absorbed causing a decrease in voltage on a photodiode measuring its intensity. Modulating the frequency of our probe, we should expect this voltage dip to increase as we move towards resonance and decrease as we move away (see Figure 3.8).
Using the offset voltage of our photodiode plus the voltage of background light as our zero-point, the absorption can be calculated as follows

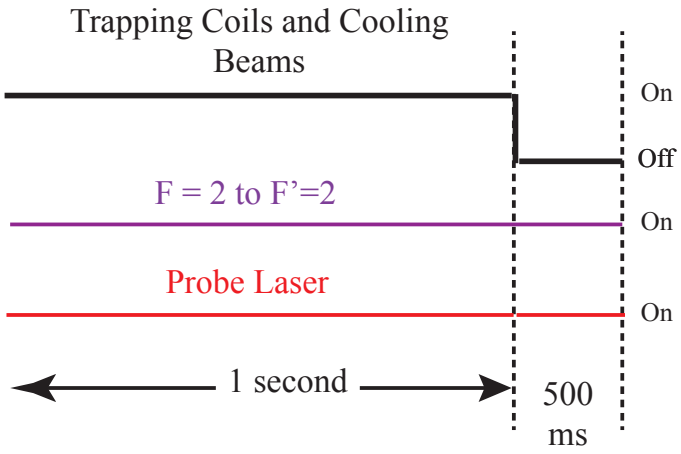

Figure 3.7: The trapping coils and cooling beams are shut off. Since the probe beam and F=2 to F'=2 are continuously on, if the probe is absorbed once these devices are shut off, there should be a drop in voltage on the photodiode measuring the probe laser power.

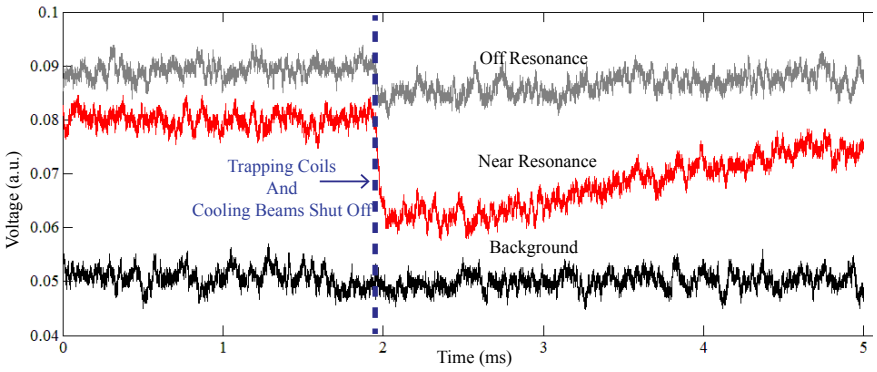

Figure 3.8: When the MOT is shut off, the perturbing effects of the trapping coils and cooling beams disappear. Therefore, the atoms will now absorb light addressing the natural atomic resonance. In our case, the atoms now absorb our probe laser addressing the F=1 to F'=1 transition. However, as time progresses, the atoms thermally expand. Since the beam is now hitting less atoms, the absorption will decrease until the atoms have completely diffused

.

$$\text{Abs} = \frac{\text{Peak Voltage} - \text{Dip Voltage}}{\text{Peak Voltage} - \text{Background Voltage}}. \tag{3.24}$$

Taking a measurements at numerous frequency values, via adjusting the AOM, we can reconstruct the absorption spectrum of our transition. The results are in Figure 3.9.

The transmission spectrum shown here is simply 1 − Absorption. If we were to plot absorption it would then take the shape of a Gaussian for room temperature atoms and

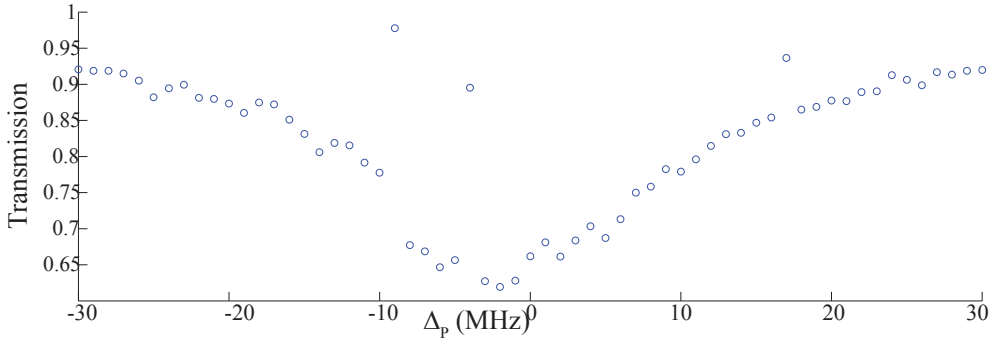

Figure 3.9: Calculating the absorption from the oscilloscope readout spanning a range of frequencies for our probe laser, we can reconstruct its absorption spectrum

.

approach a Lorentzian as the temperature goes to 0 K. The linewidth of the spectrum is given by the full width half maximum (FWHM). For room temperature rubidium atoms, Doppler Broadening gives a linewidth of approximately 500 MHz [23]. The natural linewidth of rubidium is 6MHz [9]. Figure 3.9 shows a linewidth of approximately 20 MHz. This suggests that we are close to the cooling limit of our atoms.

We cannot see EIT for probe and control beams that are not coaligned. This suggests that our atoms are not cold enough. In other words, our linewidth is broadened too much by Doppler broadening. This results in a larger range of velocity classes for our atoms. Because of this, the resonance frequency difference for atoms moving towards each beam compared to atoms moving away will also be larger. This increase in resonance frequency difference holds true for all in different velocity classes, hence a larger linewidth. Since non-coaligned probe and control beams will see atoms in different velocity classes, the excited of the EIT Λ system will exist at different energy levels for both beams. This prevents the necessary two-photon detuning required for EIT.

With cold enough atoms, the linewidth should be narrow enough to prevent this disparate velocity spread. This is desirable for the future of the experiment as we plan to couple the probe field to an optical cavity that surrounds the atoms in order to increase light-matter interaction(see Figure 2.15). If the control field has to be coaligned with the probe field then it would also have to be coupled to the optical cavity. This would add unnecessary complexity to the experiment; it would be much easier to send the control field into the atoms from another angle than the probe.

3.3.2 EIT

We originally attempted to observe EIT without the probe and control co-aligned as seen

in Figure 3.10a:

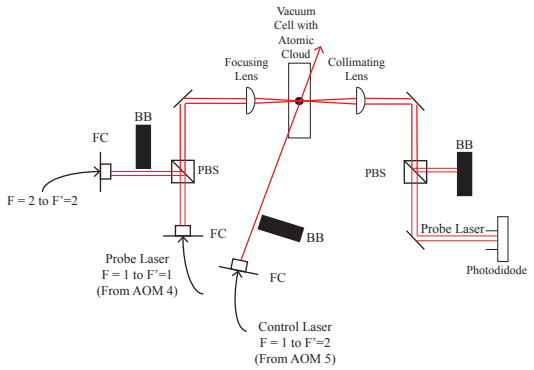

(a) Moving the beam blocks in front of the control or the F=2 to F'=2 beams, allowed us to measure the effect each beam had on the absorption spectrum of the probe.

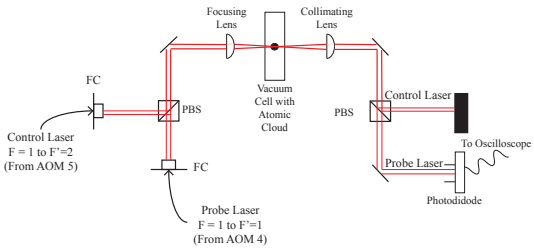

(b) We were only able to see EIT effects when the control laser was coaligned with the probe laser.

Figure 3.10: Setups for EIT measurements

Using the same pulsing set-up as the absorption measurements in the previous section, but with the F=2 to F'=2 replaced with the F=2 to F'=1, we would vary the frequency of the probe and measure the absorption spectrum. Unlike the previous measurement where the absorption spectrum continually decrease then increases, if EIT is present we would expect to see a sharp spike in near the middle of the curve. After numerous attempts, we were only able to produce a normal absorption curve as seen in Figure 3.11.

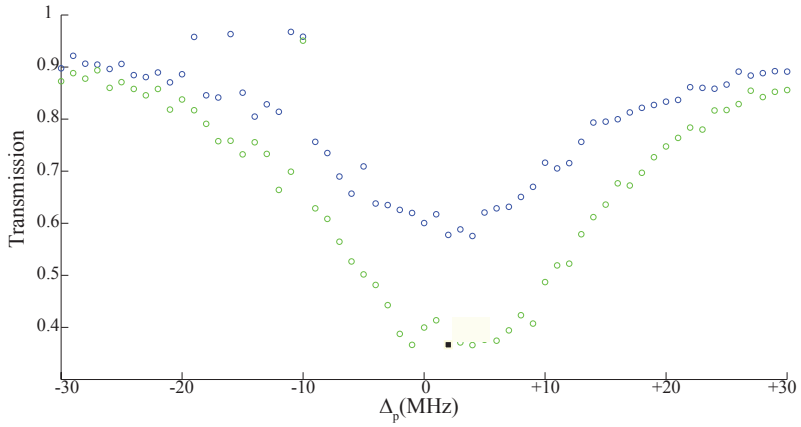

Figure 3.11: Comparison of F=1 to F'=1 absorption with F=2 to F'=2, green, and F=2 to F'=1, blue, acting as the repumping beams.

The reason behind the design of this failed set-up was being able to measure the absorption spectrum of our probe with EIT conditions (F=2 to F'=1) and without (F=2 to F'=2) at the same time, allowing us to compare and look for possible EIT characteristics.

Thinking that lack of co-alignment was preventing EIT conditions, the F=2 to F'=2 was removed from its co-aligned position and replaced with the control beam addressing the F=2 to F'=1 transition. With this setup (see Figure 3.10b), it was noticed that at very specific frequencies of the probe beam, the oscilloscope voltage signal of the probe power displayed some peculiar behavior. We did not see the sudden drop in voltage as the trapping coils and cooling beams are turned off, followed by a slowly increasing voltage as the atoms diffuse as seen in Figure 3.8. Instead, the drop in voltage was followed by a sudden peak in voltage, followed by a smooth increase in voltage as the atoms thermally expanded (see Figure 3.12). As explained before, a larger voltage dip corresponds to greater absorption, so this peak must represent some period of less absorption, i.e., transparency.

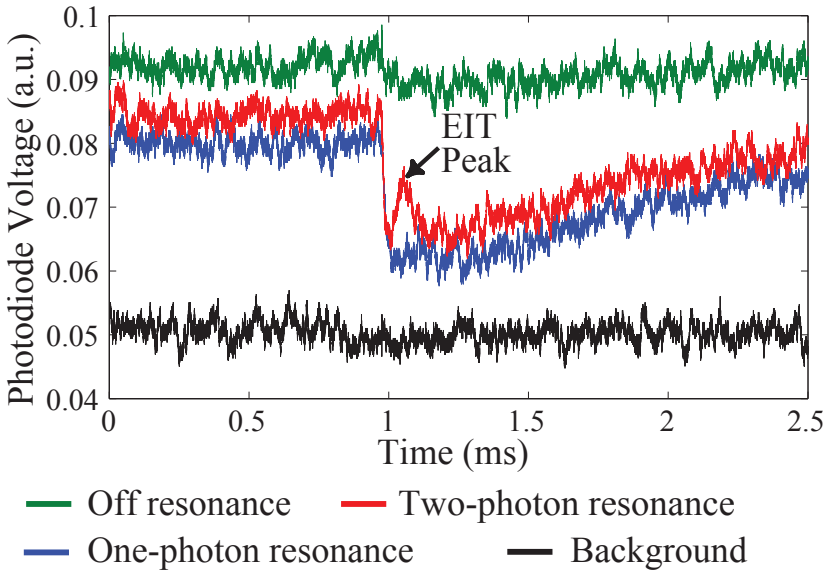

Figure 3.12: A sudden peak in voltage during the absorption process of the atoms suggests transparency.

Even more interesting was that this peak occurred at two different probe frequencies. To explore this further, a full absorption spectrum was taken by scanning the probe frequency. As our scope data suggested, we indeed see two evident transparency peaks in our absorption spectrum (see Figure 3.13).

The theoretical treatment of EIT shows transparency over a small, yet fixed frequency range of approximately 1 MHz (see Figure 3.2). However, our oscilloscope data shows transparency only at a specific time even for a fixed frequency (see Figure 3.12). What makes this transparency also a function of time? This question can be answered by comparing the linewidth of absorption versus EIT. As the atoms expand their velocity increases. This slightly expands their linewidth, making them resonant over a larger range of frequencies. However, compared to the linewidth of absorption, approximately 20 MHz, the majority of

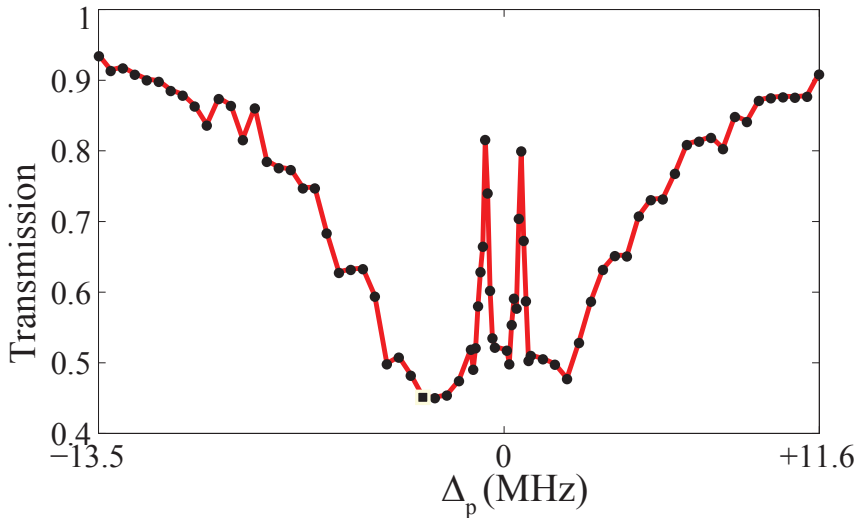

Figure 3.13: Absorption Spectrum with two clear peaks in transmission.

the atoms still remain on or near resonance with laser. This is shown by the constant level of absorption seen over the first 0.5 ms Figure 3.12. The linewidth of EIT is much smaller than the 20MHz linewidth of our absorption. Therefore, only atoms in just the right velocity class will be on two-photon resonance and experience EIT. In our case, from Figure 3.12, this velocity corresponds to the expanding atoms at approximately 0.1 ms after the trapping coils and cooling beams are shut off. In both cases, the absorption decrease later in time because the optical depth is decreasing as the atoms expand. This our lab's interpretation of the EIT peak in time. However, it is speculative and further investigation is needed to confirm these ideas.

In regards to seeing double peaks, this goes against the theoretical prediction of one EIT peak (see Figure 3.2)! We were quite perplexed by this for sometime, but eventually hypothesized that they were caused by Zeeman splitting, as this splitting can lead to more than one lambda configuration. Since our trapping coils are off during each absorption measurement, the Zeeman splitting must be a result of spurious magnetic fields. The Zeeman splitting for the transitions we are addressing is 0.93GHz/Gauss [9]. We believed that this could correspond to Zeeman states experiencing a magnetic field equivalent to that of the Earth, ≈ 0.5 Gauss.

Eliminating Double Peak

To explore this hypothesis, we constructed a setup of Helmholtz coils around our setup. Since a pair of Helmholtz coils produces a relatively constant magnetic field, three pairs of coils in each dimension are efficient to cancel out any external magnetic fields.

Our preliminary measurements involved measuring the magnetic field at the center of the atomic ensemble with a Gaussmeter. Since our entire vacuum system was temporarily removed at the time, this was easy. These measurements supported our idea that the Earth's magnetic field was the culprit, as the major field we measured pointed towards the ground. The goal of these measurements was to give us a place to start with the currents we applied to our Helmholtz coils.

Our end goal was to converge the two peaks into one. Ultimately, this would involve recreating the EIT absorption spectrum in figure 3.13 for numerous magnetic field parameters, and hopefully finding a pattern that decreased the frequency separation between the peaks. Unfortunately, our old method of manually recording an average oscilloscope readout of the voltage for a large number of probe frequencies was cumbersome and lengthy. We needed a quicker way to determine if our magnetic fields were leading us in the right direction. This was accomplished with a function generator.

Connecting our AOM driver to a wavefunction generator, we could ramp over the voltage modulating the frequency of our AOM controlling the probe laser. This is analogous to what we did before manually, except we cover a continuous range of frequencies over a time period before the atoms thermally expand and we lose absorption. Unlike manually changing the frequencies, our oscilloscope data doesn't just tell us the absorption at a fixed frequency and how this absorption changes as the atoms expand. Since we are ramping the frequency, the time on the oscilloscope corresponds to different frequencies. Therefore, if we ramp our frequencies before the atoms expand, we recreate our entire EIT spectrum in Figure 3.13, but in real time (see results in Figure 3.15). From previous absorption graphs we noticed that 100μs after the MOT is shut off, there was max absorption for $300 - 400\mu$s before the atoms began to expand and absorption decreased. Therefore, we began our ramp at a delay of 100μs with length of 400μs, as seen in Figure 3.14.

Doing this for several magnetic fields required readjusting the alignment of the cooling beams and probe/control beams since the magnetic field moved the position of the atomic ensemble. Alignment was considered satisfactory when the voltage dip gave an absorption of $\approx$ 50-60%, as this seemed to be the maximum we could obtain (see Figure 3.13). Focusing on the z-magnetic field to eliminate the effects of the Earth's magnetic field we were able to bring this peaks together and even reverse their positions. These results are seen in Figure 3.15 and Figure 3.16.

From (Figure 2.2), we see that a magnetic field, B, zeeman splits the magnetic states. For $B > 0$ this shifts the $m_f > 0$ states higher in energy and the m_f states lower. The opposite is true for $B < 0$. This splitting in energy increases linearly with magnetic field. In our case, we are applying an upwards linear magnetic field to cancel the downwards

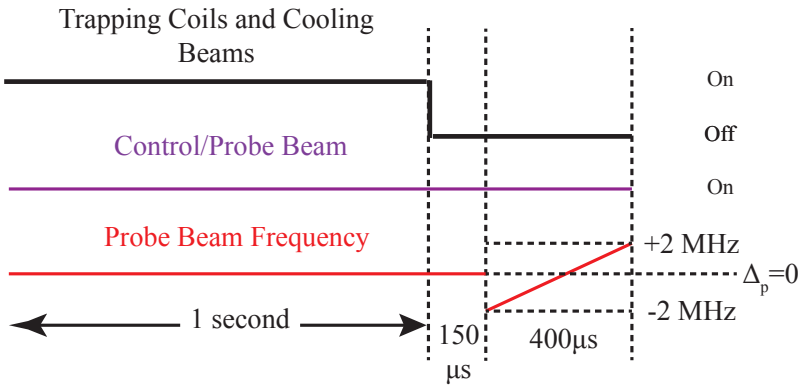

Figure 3.14: In the previous EIT measurement the frequency of the probe and control was fixed for each measurement. Here, the control frequency is fixed but we vary the frequency of the probe over a span of 400μs. Since the control frequency is near zero-detuning, passing the probe frequency through zero detuning should reveal EIT somewhere along the frequency ramp. This allows us to observe any EIT peaks in real time.

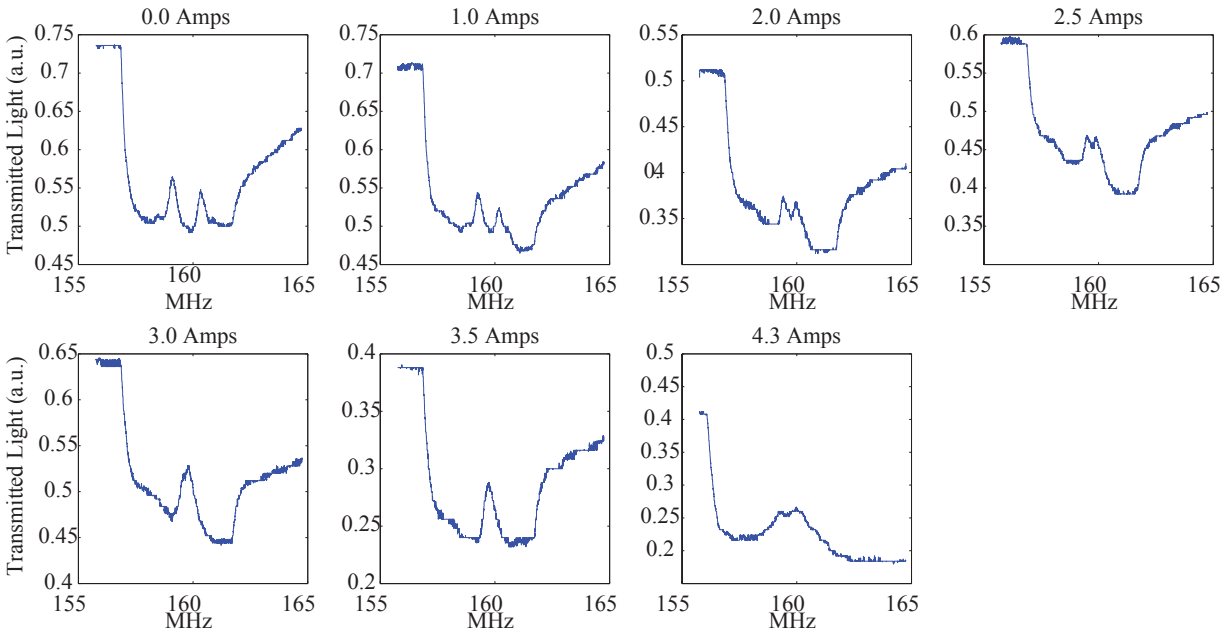

Figure 3.15: Increasing the Magnetic field we were able to cancel out the effect of the earth's magnetic field and even reverse field direction.

linear magnetic field of the Earth. Because of this, we should expect to see transitions at different energies, with separations that decreases linearly as the magnetic field approaches zero. Because of the dependence of the splitting on direction of the field, with a strong enough magnetic field we should even be able to reverse the position of the peaks. That is, the higher frequency peak becomes lower and the lower frequency peak higher. This is

indeed what we saw (see Figure 3.16) as the separation between the peaks decreases linearly as the magnetic field increases, with the peaks eventually reversing positions as we went from an Earth dominating field to a Helmholtz dominating field.

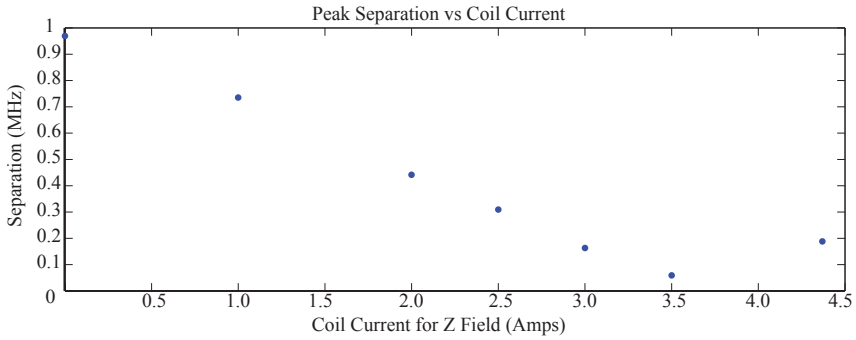

Figure 3.16: The separation decreases linearly with current in our Helmholtz coils

Chapter 4

Kerr Nonlinearites and Cross Phase Modulation

EIT drastically alters how light interacts with an atomic medium. The index of refraction can be manipulated enough to slow down light to a few meters per second within the medium [20]. This is a linear effect on the atomic medium and is related to the linear electric susceptibility χ, defined by $P = \epsilon_o \chi \boldsymbol{E}$, where $\boldsymbol{P}$ is the polarization of the medium and $\boldsymbol{E}$ the electric field. However, as will be discussed in this chapter, this polarization can be expanded to include nonlinear terms that also impact the atom's optical properties. Of importance here is the optical Kerr effect, which results in one light wave modulating the phase of another light wave. Slight modification of EIT can enhance this nonlinear effect, leading to greater cross phase modulation (XPM) between two light fields [19].

4.1 Kerr Nonlinearities

For electric fields $\mathcal{E}$ comparable to intraatomic fields the relationship between polarization and electric field includes nonlinear terms that are not negligible. The polarization of an atomic medium in such a field can be written as a Taylor series about $\mathcal{E} = 0$ as

$$P = a_1 \mathcal{E} + \frac{1}{2} a_2 \mathcal{E}^2 + \frac{1}{6} a_3 \mathcal{E}^3 \tag{4.1}$$

where a_1, a_2, a_3 are the first, second, and third derivatives of P with respect to $\mathcal{E}$ evaluated at $\mathcal{E} = 0$; these are characteristic constants of the medium. Usually, this is written as

$$P = \epsilon_o \chi \mathcal{E} + 2d\mathcal{E}^2 + 4\chi^{(3)} \mathcal{E}^3 \tag{4.2}$$

where χ is the linear susceptibility related to dispersion and absorption, $2d = \frac{1}{4} a^2$ and

$4\chi^{(3)} = \frac{1}{24}a^3$ are the constants characterizing the strength of the second and third order nonlinearity, respectively (Here we have treated everything as scalars. In reality, $\mathcal{E}$ is a vector and χ is a tensor.) [16]. Since our rubidium cloud is centrosymmetric, the second order term vanishes since the polarization must exactly reverse when the electric field reverses. The polarization therefore becomes

$$P = \epsilon_o \chi \mathcal{E} + 4\chi^{(3)}\mathcal{E}^3, \tag{4.3}$$

leaving $\chi^{(3)}$ as the dominant nonlinear term.

To understand how light interacts with this medium we will consider a monochromatic optical field of angular frequency ω and complex amplitude $E(\omega)$ described by

$$\mathcal{E}(t) = \mathrm{Re}[E(\omega)e^{i\omega t}] = \frac{1}{2}[E(\omega)e^{i\omega t} + E^*(\omega)e^{-i\omega t}]. \tag{4.4}$$

For this field it can be shown that the nonlinear polarization term in (4.3) contains a frequency component at ω

$$P_{NL}(\omega) = 3\chi^{(3)}|E(\omega)|^2 E(\omega). \tag{4.5}$$

The presence of this nonlinear component in turn modifies the linear susceptibility by an amount

$$\epsilon_o \Delta\chi = \frac{P_{NL}(\omega)}{E(\omega)} = 3\chi^{(3)}|E(\omega)|^2 = 6\chi^{(3)} I, \tag{4.6}$$

where $I = |E(\omega)|^2/2\eta$ is the optical intensity of our wave in our medium refractive index n and impedance $\eta = \eta_o/n$ where η_o is the impedance of free space. Through the relation $n^2 = 1 + \chi$, this change in susceptibility results in a change of the refractive index of

$$\Delta n = \frac{\Delta\chi}{2n} = \frac{3\eta}{\epsilon_o n}\chi^{(3)} I = \frac{3\eta_o}{n^2\epsilon_o}\chi^{(3)} I = n_2 I \tag{4.7}$$

where we have defined $n_2 = \frac{3\eta_o}{n^2\epsilon_o}\chi^{(3)}$, this n_2 term is called the Kerr nonlinearity.

We see that the index of refraction seen by a wave in a Kerr Medium is modulated by its own intensity, such that its index of refraction is described by

$$n(I) = n + n_2 I \tag{4.8}$$

this is known as the Optical Kerr Effect, and it causes the wave travelling through the medium to self-modulate its phase. The phase shift incurred by the wave initial wave vector k_o travelling through a Kerr medium of length L is

$$\phi = -n(I)k_o L = 2\pi n(I)L/\lambda_o = -2\pi(n + n_2 I)L/\lambda_o. \tag{4.9}$$

From this we see that, compared to a purely linear medium, the nonlinear term results in a phase shift modulation of

$$\Delta\phi_{SPM} = -2\pi n_2 \frac{L}{\lambda_o} I \tag{4.10}$$

Of interest to this thesis is not only the phase modulation of one wave, but what happens when two light waves encounter a Kerr Medium. The results follow a similar derivation.

For two monochromatic fields consisting of frequencies ω_1 and ω_2 the electric field now takes the form

$$\mathcal{E}(t) = \mathrm{Re}[E(\omega_1)e^{i\omega_1 t}] + \mathrm{Re}[E(\omega_2)e^{i\omega_2 t}] \tag{4.11}$$

As before, substituting this into the nonlinear term of (4.3) the polarization has a nonlinear component at ω_1 of

$$\begin{aligned} P_{NL}(\omega_1) &= \chi^{(3)}[3|E(\omega_1)|^2 + 6|E(\omega_2)|^2]E(\omega_1) \\ &= \chi^{(3)}[6I_1\eta + 12I_2\eta] \end{aligned} \tag{4.12}$$

Following the steps from (4.5)-(4.7), with the same definitions of n_2 and I, except with waves of two different intensities, we can then show from (4.12) that our phase shift is

$$\Delta n = n_2 I_1 + 2n_2 I_2, \tag{4.13}$$

where we have assumed both beams experience the same index of refraction.

We see that the first term of our index shift is the same intensity dependent shift expected from self-phase modulation of our ω_1 wave. However, the second term shows that our ω_1 wave also experiences an index shift from the intensity of the ω_2 wave. This is called cross-phase modulation (XPM), as the intensity of a second wave can control the phase of another wave by changing the refractive index seen by wave 1. As expected, the total phase shift the ω_1 wave would experience in this situation includes the traditional linear phase shift, the phase shift from SPM, and the phase shift from XPM. For two waves of identical initial wave vector, $k_o = k_{1_o} = k_{2_o}$, traversing the same length, $L = L_1 = L_2$ of the Kerr medium, this gives a total phase shift of:

$$\phi = -n(I)k_o L = 2\pi n(I)L/\lambda_o = -2\pi(n + n_2 I_1 + 2n_2 I_2)\frac{L}{\lambda_o}. \tag{4.14}$$

Compared to (4.9), we see XPM alters the ω_1 wave phase shift expected from linear effects and SPM by an amount

$$\Delta\phi_{XPM} = -4\pi n_2 \frac{L}{\lambda_o} I_2. \tag{4.15}$$

The two experimentally adjustable factors for increasing or decreasing the size of this phase shift are the length of the Kerr Medium and the Intensity of the cross-phase modulating wave, I_2. Since the size of experimentally obtained atomic clouds are confined within 1-2 orders of relative magnitude, they do not provide much flexibility in dramatically altering the size of this phase shift. The leaves the intensity of the second wave as the leading factor in controlling these phase shifts.

4.2 Increasing XPM Phase Shifts

One of the elusive goals of QIP, and the ultimate motivation of this thesis, is a phase shift exceeding π rad of a single photon light field by another single photon light field. We have shown in the last section that XPM can use one light field to modulate the phase of another light field. However, this is not the final piece of the puzzle. In typical three-level systems for XPM (see Figure 4.1), the Kerr nonlinearity for gaseous alkali metals is on the order of $10^{-15}\mathrm{m}^2/\mathrm{W}$. From (4.15), the phase shift is proportional to the intensity. For such a small nonlinearity, significant phase shifts can therefore only be achieved with intense laser pulses, more than 10 orders of magnitude larger than a single photon light field. Clearly, to reach the QIP goal above, we must combine with XPM with another tool to increase the Kerr nonlinearity. This can be accomplished with EIT.

In 1996, Schmidt and Imamoglu [19] proposed EIT as a way to drastically increase Kerr nonlinearities. Compared to a conventional three-level XPM scheme (see Figure 4.1), they proposed XPM through an N-type EIT scheme (see Figure 4.2). In an N-type EIT scheme, a signal field ω_s is added addressing a transition between $|2\rangle$ of the previous 3-level EIT Λ scheme to a new state, $|4\rangle$, thus transforming the system to a 4-level N-type system. This signal field is used to modulate the phase of the probe field.

For each system the nonlinear coefficient was determined as

$$\mathrm{Re}[\chi^{(3)}]_{3-level} = \frac{N|\mu_{gi}|^2|\mu_{iu}|^2}{8\epsilon_o\hbar^3}\frac{1}{\Delta\omega_a^2\Delta\omega_b} \tag{4.16}$$

$$\mathrm{Re}[\chi^{(3)}]_{EIT} = \frac{N|\mu_{13}|^2|\mu_{24}|^2}{2\epsilon_o\hbar^3}\frac{\Gamma_4}{\Omega_c^2\Delta\omega_s}, \tag{4.17}$$

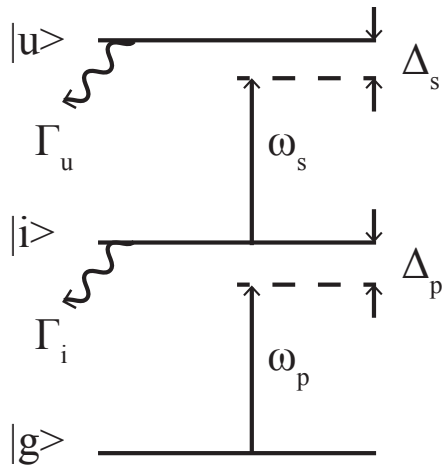

Figure 4.1: Conventional 3-level Scheme for XPM: ω_p is the probe laser whose phase will be modulated by the signal laser, ω_s. As defined before, $\Delta\omega$ represents detuning from atomic resonance and Γ is the decay rate.

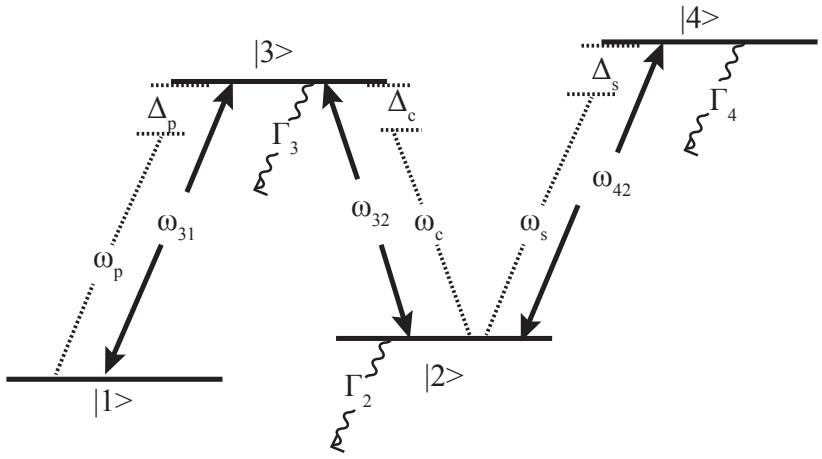

Figure 4.2: Proposed EIT Scheme for Giant Kerr Nonlinearities: Introducing a new level $|4\rangle$ to the previously defined EIT Lambda, Λ, system creates a 4-level N-type system. The new level $|4\rangle$ is addressed from $|2\rangle$ using a signal laser, ω_s. This signal laser acts as the phase-modulator of the probe laser, ω_s, creating large Kerr nonlinearities.

where N is the atomic density, μ_{ij} are the dipole operators, Γ and $\Delta\omega$ follow the definitions in the previous figures.

From these two equations the main difference is that for the 3-level scheme the detuning from the intermediate level $\Delta\omega_a^2$ is replaced in the EIT level scheme by the Rabi frequency Ω_c^2. The Rabi frequency can be chosen to be much smaller than the one-photon detuning, as the detuning is limited by the linewidth. Because of this, the nonlinear coefficient can drastically increase [19]. Schmidt and Imamoglu demonstrated this increase through a calculation with a 1-cm long sodium cell with atomic density $N = 10^{12}\text{cm}^{-3}$. Carrying out the same calculation

for both schemes, they found that obtaining a 10^o phase shift for the EIT scheme required a field intensity of $I_{EIT} = 1.0 \times 10^{-7}\text{W/cm}^2$. The same phase shift for the conventional 3-level scheme required an intensity $I_{3-level} = 3.3 \times 10^2\text{W/cm}^2$. The resulting nonlinearites ($\text{Re}[\chi^{(3)}]$) were $3.3 \times 10^{-6}\text{m}^2/\text{V}^2$ and $1.0 \times 10^{-15}\text{m}^2/\text{V}^2$ for EIT and conventional XPM, respectively. Comparing the two schemes, the EIT scheme has a nonlinearity increased by 9 orders of magnitude, resulting in the same phase shift for an intensity 9 orders of magnitude less. This is the motivation for developing an XPM-EIT system.

These equations and calculated values show a large increase in the Kerr nonlinearity, but do not physically reveal what is occurring. A more intuitive picture can be seen through the dispersion created by EIT. This is seen in the bottom plot of Figure 3.2, where the imaginary part of χ determining index of refraction is shown as a function of two-photon detuning of the probe/control fields. From Figure 3.2 we see very steep dispersion around zero detuning. This means very small changes in the two-photon detuning can lead to large changes in the refractive index. From Figure 4.2, we see our signal field coupled to states $|2\rangle$ and $|4\rangle$. This causes an AC Stark shift in our $|2\rangle$ state. This will slightly modify the two-photon detuning needed for two-photon resonance, as we are modifying the resonance frequency of our control field. As we stated, this change in detuning results in a large change for the refractive index. Therefore, the signal field modifies the control field, which modifies our EIT properties, which in turn results in the probe field experiencing a large change in the refractive index. This ultimately leads to the large phase modulation of our probe field [20].

4.2.1 N-Type Implementation

As shown in Figure 4.2, observing this N-Type XPM requires an addition to our EIT level scheme. This can be accomplished by addressing the F=2 to F'=3 transition in our rubidium atoms (see Figure 4.3). Fortunately, the previously constructed absorption imaging setup using AOM3 (see Figure 2.9) addresses this transition, so no additional AOMs are required.

Using the same beam configuration to image the atoms (see Figure 2.11), our goal was to observe an effect on our EIT spectrum when the atoms interacted with the F=2 to F'=3 beam. To do this, the same experimental setup for converging the EIT peaks, (see section 3.3.2, Eliminating Double Peaks) was used. As explained before, this setup ramped through our probe detuning over a span of $400\mu s$, going below and above two photon resonance by 2 MHz. The motivation for this ramping was to image our characteristic transparency peaks in the EIT spectrum in real time on an oscilloscope. With a current of 3.5 Amps in our helmholtz coils, a Z magnetic field converged these peaks to one larger EIT peak. The

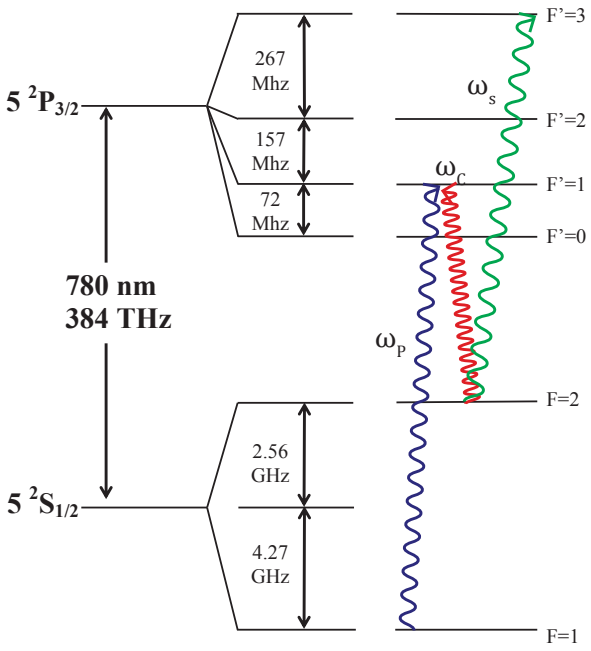

Figure 4.3: Addressing the F=2 to F'=3 transition atomically implements the theoretical N-Type scheme (see figure 4.2) needed for increased Kerr Nonlinearities

measurement here consisted of observing the converged transparency peak with and without the presence of the F=2 to F'=3 laser. As we see in Figure 4.4, as the power of the F=2 to F'=3 beam is increased, there is a noticeable effect on the EIT peak with and without this beam.

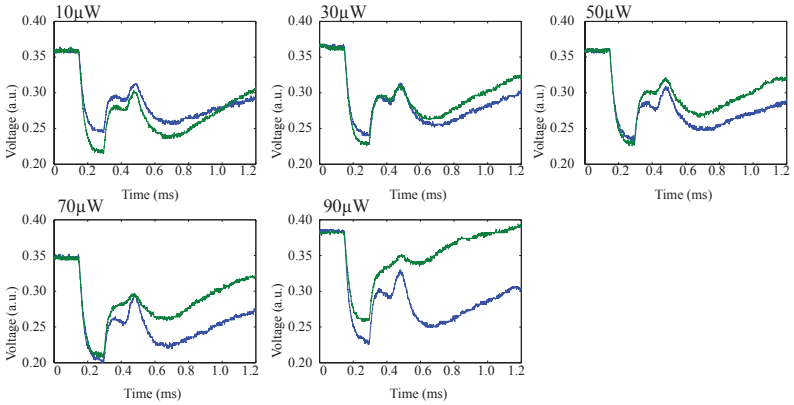

Figure 4.4: Each plot shows the EIT spectrum obtained via ramping the probe detuning (see Figure 3.14. The green plot is the spectrum with our F=2 to F'=3 signal field, whereas the blue plot is the EIT spectrum without the signal field. As the signal power is increased from 10-90 μW, the effect on the transparency peak becomes larger.

As explained in chapter 3, EIT can be used to greatly reduce the group velocity of light.

An important consequence of this slowdown is the spatial compression of pulses of light. This is because when a pulse enters an EIT medium, the front end of the pulse travels more slowly as it enters the medium first. Still not arrived at the medium, the back end of the pulse is traveling near the speed of light. The back end thus catches up to the slowly moving front end, compressing the width of the pulse. Measuring the time pulses sent through the atomic medium reach a photodetector thus gives us another way to see if EIT conditions have been modified.

The pulses are Gaussian with a FWHM of 5 μs, created by a wavefunction generator that modulates the AOM generating the laser at the transition frequency of F=1 to F'=1. They are sent through the atomic medium at the time the absorption signal of our atoms shows a maximum transparency peak. To find this time we look at the continuous EIT signal like that shown in Figure 3.12, and send the signal at the same time we see this peak. However, this time is not quite correct, as the continuous absorption signal seen in Figure 3.12 heats up the atoms faster, meaning their velocities will more quickly reach those required for the atoms to see the light at two-photon resonance. In this measurement, since we are just sending pulsed signals, the atoms expand more slowly, meaning this condition is not met until later in time. By increasing the time difference with respect to the triggering point, we can observe a peak that is larger than the rest as it is more transparent (see Figure 4.7). This corresponds to our EIT peak in the pulsed regime. As seen in Figure 4.5, the pulse sent during normal EIT conditions suffers the compression explained previously, with the center arriving later in time than the pulse experiencing no EIT. We see that sending a pulse while the F=2 to F'=3 N-type beam is effecting the medium modifies the EIT pulse.

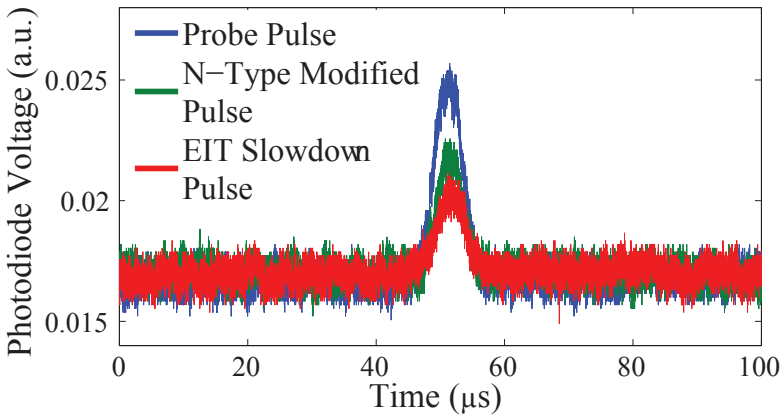

Figure 4.5: Pulse arrival for no EIT, EIT, and N-type modified EIT. The time is measured with respect to an arbitrary triggering point that occurs after the MOT trapping coils and cooling beams are turned off.

The measurements here focused on finding changes in the EIT properties of our system

by observing the effects the N-type signal beam had on the EIT transparency peak as well as its effect on the slowdown of pulses. Expected from other experiments [26], an N-type setup capable of XPM will lessen the height of the transparency peak. As seen in Figure 4.4, this is what we saw. Lessening of this transparency peak also results in less effect on reduction of group velocity. Therefore, an N-type pulse should arrive sooner than an EIT pulse. Again, from Figure 4.5, we believe to see this effect. With these observations, the next logical step was to characterize the phase shift caused by this modulation of the EIT spectrum through the signal field.

4.3 Measurement of Phase Shifts

We need some way to characterize our cross-phase modulation. This requires measuring the phase of the probe field after exiting the atomic ensemble of cold rubidium, where it undergoes manipulation by the signal field. Comparing this to its phase without passage through the ensemble tells us the phase modulation imparted by the signal field. This is possible through a technique known as balanced homodyne tomography.

4.3.1 Electric Field Quadratures

We can define the Hamiltonian for our single-mode electromagnetic field in terms of annihilation and creation operators as (for a more detailed explanation leading up to this see references [27], [24], or [25])

$$H = \hbar\omega\left(\hat{a}^\dagger\hat{a} + 1/2\right). \tag{4.18}$$

From this we can create an electric field operator:

$$\hat{\mathcal{E}}(z,t) = \mathcal{E}_\omega(\hat{a} + \hat{a}^\dagger)\sin kz, \tag{4.19}$$

where $\mathcal{E}_\omega = [\hbar\omega/\epsilon_o V]^{1/2}$ is the "electric field per photon" which has a single-mode field oscillation frequency ω, wave number k, and is in a cavity of volume V [24]. However, we cannot measure the electric field in this form as $\hat{a}$ and $\hat{a}^\dagger$ are not Hermitian operators. Nonetheless, from linear combinations we can form Hermitian operators, $\hat{X}_1$ and $\hat{X}_2$, called quadratures

$$\hat{X}_1 = \frac{1}{\sqrt{2}}\left(\hat{a} + \hat{a}^\dagger\right) \qquad \hat{X}_2 = \frac{i}{\sqrt{2}}\left(\hat{a} - \hat{a}^\dagger\right), \tag{4.20}$$

which are 90^o out of phase with each other. Including the time dependence of our annihilation and creation operators we can recast the electric field operator as [25]

$$\hat{\mathcal{E}}(z,t) = \mathcal{E}_\omega(\hat{a}e^{i\omega t} + \hat{a}^\dagger e^{-i\omega t})\sin kz \tag{4.21}$$

$$= \sqrt{2}\mathcal{E}_\omega \sin kz[\hat{X}_1 \cos\omega t + \hat{X}_2 \sin\omega t]. \tag{4.22}$$

From this we see that the electric field can be written as two Hermitian, and thus measurable, quadrature operators, $\hat{X}_1$ and $\hat{X}_2$, that are the in-phase and out-of-phase components of the electric field amplitude with respect to a reference phase.

4.3.2 Balanced Homodyne Detection

Balanced Homodyne Detection utilizes light of a known phase to "pick out" the components of this "in-phase" electric field quadrature of light. In our case, the light field whose electric field phase we want to measure is the probe field, $\mathcal{E}_p$. This is accomplished through the use of a large amplitude light wave with the same frequency, hence homodyne not heterodyne, as the probe field, but with a defined phase. Combining this large field, called the local oscillator (LO), at a beam splitter with the probe field gives two output fields [27]

$$\begin{aligned}\mathcal{E}_1 &= \frac{1}{\sqrt{2}}\left(\mathcal{E}_{LO}e^{i\phi_{LO}} + \mathcal{E}_p\right)\\ \mathcal{E}_2 &= \frac{1}{\sqrt{2}}\left(\mathcal{E}_{LO}e^{i\phi_{LO}} - \mathcal{E}_p\right).\end{aligned} \tag{4.23}$$

Splitting the probe field into its two quadrature values $\mathcal{E}_p = \mathcal{E}_p^{X_1} + i\mathcal{E}_p^{X_2}$ gives

$$\begin{aligned}\mathcal{E}_1 &= \frac{1}{\sqrt{2}}\left([\mathcal{E}_{LO}\cos\phi_{LO} + \mathcal{E}_p^{X_1}] + i[\mathcal{E}_{LO}\sin\phi_{LO} + \mathcal{E}_p^{X_2}]\right)\\ \mathcal{E}_2 &= \frac{1}{\sqrt{2}}\left([\mathcal{E}_{LO}\cos\phi_{LO} - \mathcal{E}_p^{X_1}] + i[\mathcal{E}_{LO}\sin\phi_{LO} - \mathcal{E}_p^{X_2}]\right).\end{aligned} \tag{4.24}$$

Combining these two fields on a photodiode such that their currents subtracts gives an intensity output

$$\begin{aligned}PD_{output} &\propto i_1 - i_2\\ &\propto \mathcal{E}_1\mathcal{E}_1^* - \mathcal{E}_2\mathcal{E}_2^*\\ &\propto 2\mathcal{E}_{LO}\left(\cos\phi_{LO}\mathcal{E}_p^{X_1} + \sin\phi_{LO}\mathcal{E}_p^{X_2}\right).\end{aligned} \tag{4.25}$$

The local oscillator thus gives an output proportional to the probe field quadrature at a

specific phase. If we want the full X_1 amplitude we choose $\phi_{LO} = n\pi$. For full X_2 choose $\phi_{LO} = \frac{n\pi}{2}$. For other values of ϕ_{LO}, we obtain linear combinations of X_1 and X_2 amplitudes with coefficients determined by the values of $\cos\phi_{LO}$ and $\sin\phi_{LO}$, respectively.

4.3.3 Phase Shift Caused by EIT

After experimentally constructing the Homodyne system (see Figure 4.6) a measurement was taken to measure the phase shift caused by EIT. In this case, our local oscillator is given a defined phase through the position of mirror connected to a piezo electric device. Ramping the position of this mirror allows us to then select the quadrature values of our probe field over a continuous range of phases and thus, from Equation 4.25, reconstruct its amplitude for each phase.

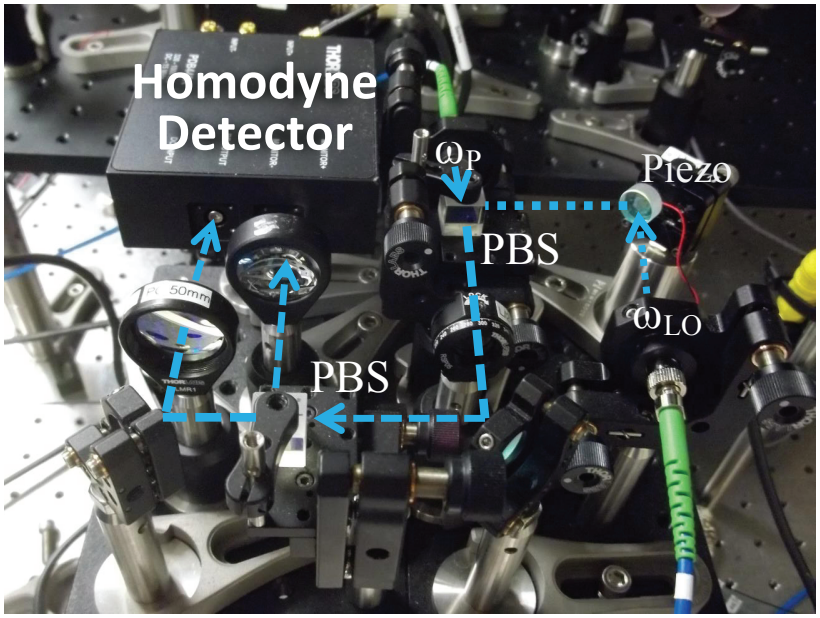

Figure 4.6: The local oscillator is joined with the probe field at a PBS. They then pass through a NonPBS into a photodiode system that creates two fields that are recorded on photodiodes. The black box has a circuit designed to subtract these currents and determines the phase from Equation 4.25

As with the slowdown pulses explained above, we needed to find where EIT existed in the pulsed regime. Instead of changing the delay as before, we found it easier to send in a train of pulses. By observing the height of each pulse, we could determine which one experienced EIT as it would be the tallest peak. As seen in Figure 4.7, this corresponds to the peak highlighted in black. As with the slowdown pulses the measurement is taken at a fixed frequency, so the image is not a full EIT spectrum in Figure 4.7, but a peak like the one in Figure 3.12. The phase of this field is then compared with a pulse passing through the

system without EIT. Due to the effect of EIT on dispersion of the atoms, we should expect a phase shift. Through our use of balanced Homodyne detection, we measured a modest phase shift.

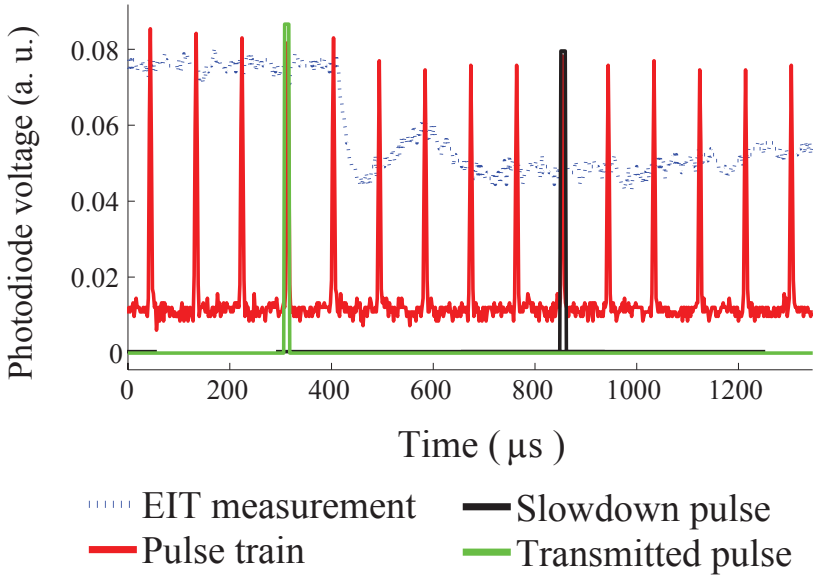

Figure 4.7: The phase of a pulse before the shut off of the (green) is compared with the phase of pulse experiencing EIT (black). The difference in phase shifts is seen in Figure 4.8

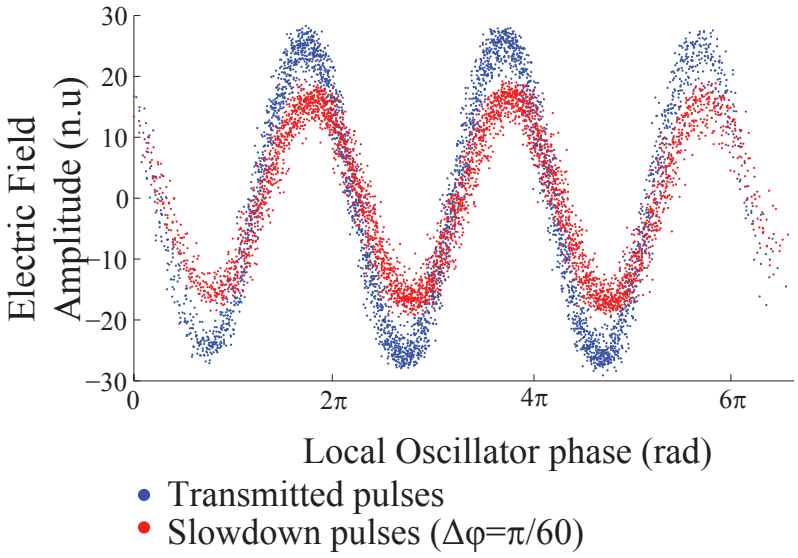

Figure 4.8: With respect to the local oscillator phase, the EIT pulses (which experience slowdown) have a modest phase change from the pulses experiencing no EIT

.

Since the phase shift was so small, we decided not to measure the effect of N-type modulation on the EIT pulse until we increased the atom-light interaction of the probe field

through the addition of a cavity. This is one of several future additions planned for this experiment, which are presented in the Outlook.

Chapter 5

Outlook

All the concepts required to construct a quantum phase gate have been demonstrated in this thesis through proof-of-principle experiments. A magneto-optical trap containing cold atoms with the correct level scheme for 3-level EIT Λ systems and 4-level N-type systems has been developed. The density of atoms is comparable to other experiments also working with cavity-atomic ensemble systems. The temperature of the atoms is approaching the Doppler limit, but should be colder in order to decrease the linewidth. This should allow the probe and control beams to still create EIT even when they are not coaligned. Nonetheless, our results suggests that our light-atom interface at its current stage is robust enough of a platform to mediate our light-atom-light interactions.

Regarding these interactions, we have successfully developed EIT in our atoms. This allows us to coherently control the optical properties of our medium. Unwanted effects that cause the EIT spectrum to deviate from theory have been eliminated. Through the development of an N-type scheme it has been demonstrated that we can manipulate EIT characteristics. As theory and experiment have shown, correct N-type modulation of EIT conditions can greatly increase the Kerr nonlinearity responsible for XPM.

A system to measure the phase shifts of this increased XPM has been developed. Using balanced homodyne detection, we have measured a small phase shift between a pulse experiencing EIT and a pulse not experiencing EIT. The next step is to measure a phase shift between a pulse experiencing EIT and one experiencing N-type modulated EIT. As explained earlier, this N-type setup could increase the Kerr nonlinear coefficient by 9 orders of magnitude; however, this still is several orders of magnitude away from working with at single-photon levels. The future of this experiment requires other techniques for increasing the Kerr nonlinearity such that π level XPM can be achieved between two single-photon pulses. The tools we will use include optical cavities and additional EIT systems.

5.1 Additional Tools to Increase XPM

5.1.1 Single-Cavity

The first addition to our current setup is the previously discussed atom-cavity system that will couple the EIT probe field to our atomic cloud. This will increase light-atom interaction, which in turn will increase the Kerr nonlinearity. To accomplish this we must make the length of the cavity equal to an integer number of half wavelengths, m, such that the length is: $L = m\lambda/2n$. This is the resonance condition of the optical cavity, which when met keeps the light in the cavity in phase during each round trip back and forth between the mirrors [11].

Maintaining the length of the cavity at resonance will require a feedback loop in which another laser coupled to the cavity continually provides feedback to a piezo-electric device that maintains the position of one of the cavity mirrors, and hence the length of the cavity. To prevent this laser from interacting with the atoms, it will operate at a different frequency than the probe laser. This adds complexity to the system in two ways. The length of the cavity must now satisfy resonance for two different wavelengths, and to measure properties of the transmitted probe laser, the feedback laser must be filtered out. Nonetheless, these are common requirements for cavity setups. The most challenging aspect of implementing this cavity will be aligning the lasers such that the cavity mode intersects the center of our trapped rubidium atoms (see Figure 2.15). If successful, this will bring use one step closer to our ultimate goal as it should increase our Kerr nonlinearity in addition to the increase given by the N-type setup.

5.1.2 Double EIT

Theoretically, it has been shown that although N-type modification of EIT can provide large Kerr nonlinearities, the increase is not large enough to achieve π phase shifts between single-photon pulses. This is why a cavity coupling our EIT probe to the atomic system will be implemented on top of our N-type scheme. The reason EIT cannot provide large enough Kerr nonlinearities is the dramatic velocity difference between the probe field, which undergoes the phase shift, and the signal field providing the phase shift [20]. This velocity difference is a result of the probe field experiencing EIT and hence a large reduction in its group velocity, while the signal field has no reduction. Double EIT can overcome this effect.

Compared to a single EIT system, a double EIT system can provide a larger nonlinear phase shift. This is because in the latter, the signal field implementing the phase shift can also undergo EIT [28]. Therefore, it can also have the same ultraslow group velocity as the

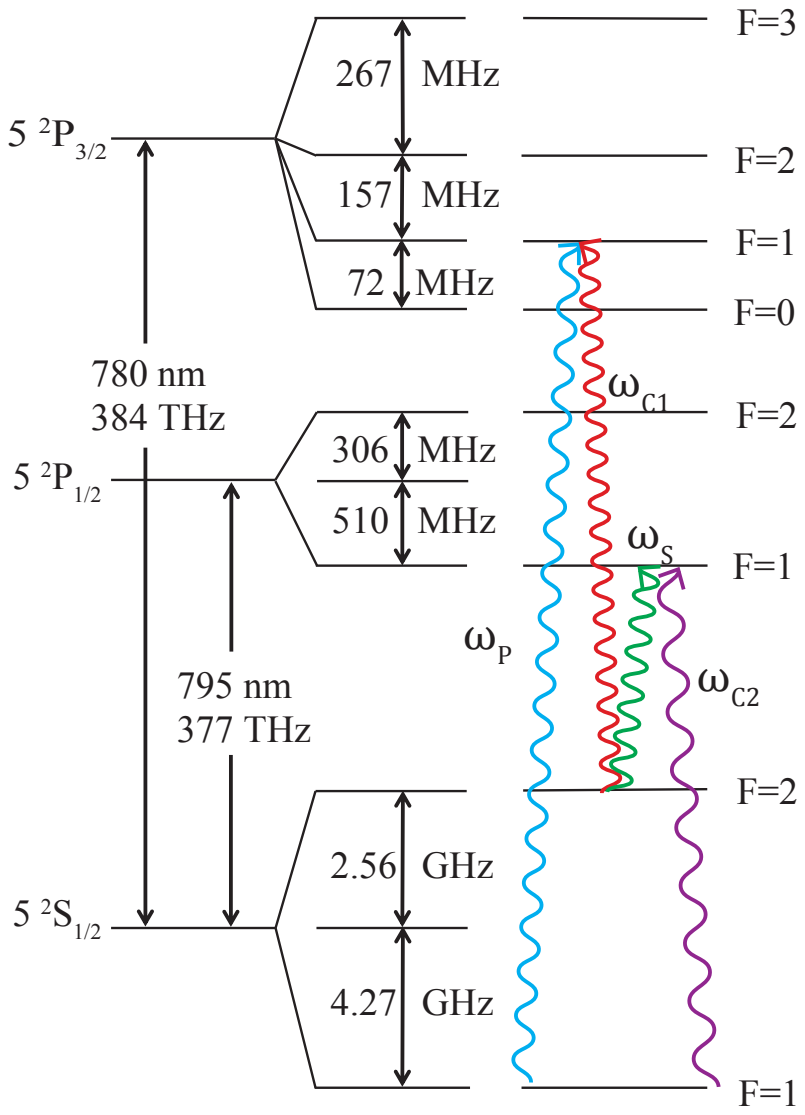

Figure 5.1: Two EIT Λ systems form an M-type scheme. The probe, ω_p, and control, $\omega_c = \omega_{c1}$ address the same transitions as before. However, the signal field addresses transitions at 795 nm. This allows the signal field, ω_s to still follow an N-type scheme required for EIT modification of the probe, but the addition of ω_{c2} creates an EIT system for our signal field. In this second EIT Λ setup the signal field is the probe and hence undergoes a reduction in its group velocity.

probe pulse. This increases the total interaction between the two pulses. Experimentally, this can be implemented by transforming our 4-level N-type into a double Λ, or M-type system (see Figure 5.1). This M-type setup will require lasers addressing the D1 = 795 nm line rubidium transition from the $5^2S_{1/2}$ to the $5^2P_{1/2}$ state. We currently already have lasers operational and locked at frequencies within this transition. As well, the necessary double-pass AOM setups to address the specific hyperfine levels and find the two-photon

detuning for EIT have also been constructed.

5.1.3 Dual Cavities

The double EIT setup increases the Kerr nonlinearity over the single EIT system that is modified by an N-type beam. However, it is still debateable in the field of QIP whether such a setup can produce π phase shifts between two single-photon pulses. Simulations undergone by our group have shown than π shifts at this single-photon level are possible by implementing a dual cavity system for both the probe field and signal field experiencing EIT. The cavity for the probe field has already been discussed. The last tool needed is then a cavity coupling the signal field to our atomic system. This would be setup like the process for the probe cavity, except orthogonal to the probe field. With this tool in place, the final construction of our phase gate would take the form shown in Figure 5.2.

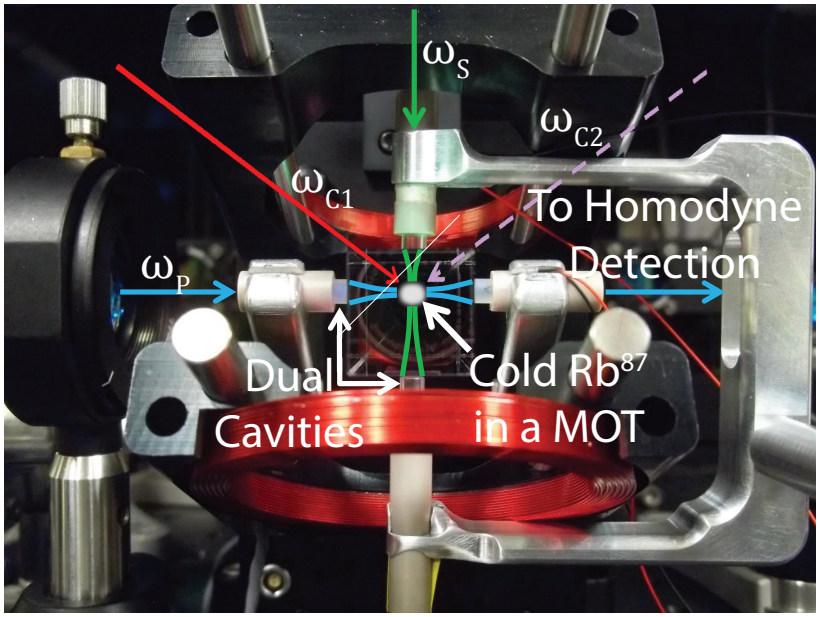

Figure 5.2: Physical setup of the ultimate design for our quantum phase gate (not yet operational, for show only). The probe field, ω_p, will be coupled to the horizontal cavity whereas the signal field, ω_s, will be coupled to a vertical cavity. With cold enough atoms the control fields ω_{c1} and ω_{c2} can be sent into the atomic system from arbitrary angles. After undergoing a phase shift in the atomic medium, the probe field will be transmitted through the cavity and into the homodyne detector.

5.2 Conclusion

This thesis has constructed the necessary components for an N-type atomic scheme capa-

ble of modifying EIT within a cold atomic ensemble. Using balanced homodyne tomography to measure phase shifts, this thesis has demonstrated optical control of electric field phase between a light field experiencing EIT and one that does not. The next step is the addition of cavities to couple the probe field undergoing EIT to the atomic ensemble. Once this is completed an M-type system should be constructed to match the group velocities of both the probe and signal field. The necessary AOM system to change the atomic scheme from N-type to M-type has been setup, but still needs characterization. The last step will be coupling of this signal field to a cavity. Such a system will be capable of providing large Kerr nonlinearites. We hope these Kerr nonlinearites are large enough such that cross-phase-modulation on the order of π rad can be achieved between the electric fields of light pulses at the single photon level. If this is successfully achieved, then once our single-photon source is operational, we can use these tools to implement a two-optical-qubit quantum logic gate. Never accomplished, this will be a significant breakthrough for QIP and an important addition for its continued success.

Bibliography

[1] Intel

[2] C. H. Bennett and G. Brassard. Quantum Cryptography: Public Key Distribution and Coin Tossing. In: Proceedings of the IEEE International Conference on Computers, Systems and Signal Processing, 175âĂŞ179, New York, (1984).

[3] S.E. Harris, J.E. Field, and A. Imamoglu. Nonlinear Optical Processes Using Electromagnetically Induced Transparency. Phys. Rev. Lett. **64**, 10 (1990).

[4] P. Zoller et. al. Quantum information processing and communication: Strategic report on current status, visions and goals for research in Europe. Eur. Phys. J. D. **36**, 203-228 (2005).

[5] M.D. Lukin. Colloguium: Trapping and Manipulating Photon States in Atomic Ensembles. Rev. Mod. Phys. **75**, (2003).

[6] C. Simon et. al. Quantum Memories: A Review Based on the European Integrated Project "Qubit Applications QAP" arxiv1003.1107v1 (2010).

[7] D.N. Matsukevich et. al. Entanglement of Remote Atomic Qubits. Phys. Rev. Lett, **96**, 030405 (2006).

[8] K. Hammerer, A. Sorensen, and E. Polzik. Quantum Interface Between Light and Atomic Ensembles. Rev. Mod. Phys. **82** (2010).

[9] D Steck. Rubidium 87 D Line Data. Los Alamos National Laboratory (2003).

[10] O.R. Frisch, Z. Phys. **86**, 42 (1933).

[11] M. Fox. Quantum Optics: An Introduction. Oxford Masters Series in Atomic, Optical, and Laser Physics. Oxford University Press (2006).

[12] C. Foot. Atomic Physics. Oxford Masters Series in Atomic, Optical, and Laser Physics. Oxford University Press (2005).

[13] D. Greif. Evaporative Cooling and Bose-Einstein Condensation of Rb-87 in a Moving-coil TOP Trap Geometry. MA Thesis, Department of Physics and Astronomy, Stony Brook University (2007).

[14] S. Albert. Cooling, Trapping, and Transport of Atom Clouds in a New BEC Appartus. MA Thesis, Department of Physics and Astronomy, Stony Brook University (2007).

[15] K. Luksch. Measurement of the number of atoms in a magneto-optical trap using absorption imaging. Diploma Thesis, Quantum Optics Group, National University of Singapore (2012).

[16] B.E.A. Saleh, M.C. Teich. Fundamentals of Photonics, Second Ed. Wiley Series in Pure and Applied Optics. John Wiley and Sons, Inc. (2007).

[17] G. Hernandez, J. Zhars, and Y. Zhu. Vacuum Rabi Splitting and Intracavity Dark-State in a Cavity-Atom System. Phys. Rev. A. **76**, 053814 (2007).

[18] E.A. Donley, T.P. Heavner, F. Levi, M.O. Tataw, and S.R. Jeffries. Double-pass acousto-optic modulator system. Rev. of Scientific Instruments **76**, 063112 (2005).

[19] H. Schmidt and A. Imamoglu. Giant Keer nonlinearities obtained by electromagnetically induced transparency. Optics Lett. **21**, 23 (1996).

[20] M. Fleischhauer, A. Imamoglu, and J.P. Marangos. Electromagnetically induced transparency: Optics in coherent media. Rev. Mod. Phys. **77**, 633 (2005).

[21] W. Erickson. Electromagnetically Induced Transparency. BA Thesis, The Division of Mathematics and Natural Sciences, Reed College (2012).

[22] E. Hecht. Optics, fourth ed. Addison-Wesley (2001).

[23] D.W. Preston. Doppler-free Saturated Absorption: Laser Spectroscopy. American Jrn. of Phys. **64**(11): 1432-1436 (1996).

[24] P. Meystre and M. Sargent III. Elements of Quantum Optics. 4th Edition. Springer (2007).

[25] C. Gerry and P. Knight. Introductory Quantum Optics. Cambridge University Press (2005).

[26] M. Bajcsy et. al. Efficient All-Optical Switching Using Slow Light within a Hollow Fiber. Phys. Rev. Lett. **102**, 203902 (2009).

[27] C. Kupchak. Complete Characterization of Quantum Optical Proccesses with a Focus on Quantum Memory. PhD Dissertation, Department of Physics and Astronomy, University of Calgary (2013).

[28] M.D. Lukin and A. Imamoglu. Nonlinear Optics and Quantum Entanglement of Ultra-slow Single Photons. Phys. Rev. Lett. **84**, 1419 (2000).